Lawrence Berkeley National Laboratory
LBL Publications

Title
A Molecular-Scale Understanding of Misorientation Toughening in Corals and Seashells

Permalink
https://escholarship.org/uc/item/69v906fz

Journal
Advanced Materials, 35(28)

ISSN
0935-9648

Authors

Lew, Andrew J
Stifler, Cayla A
Tits, Alexandra
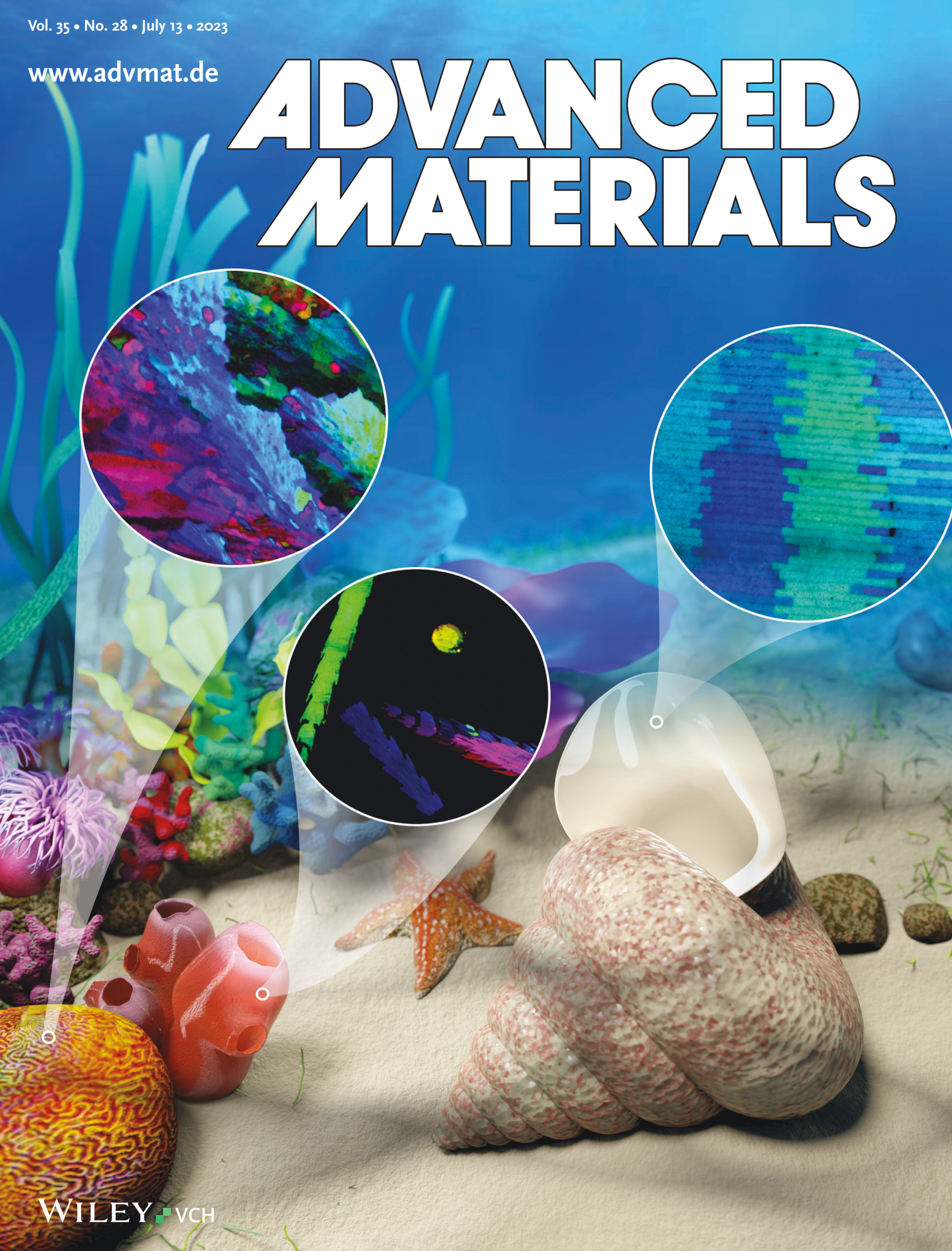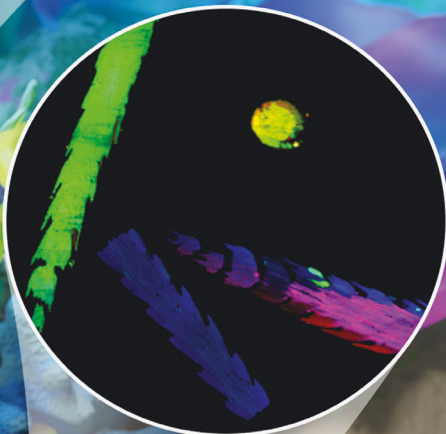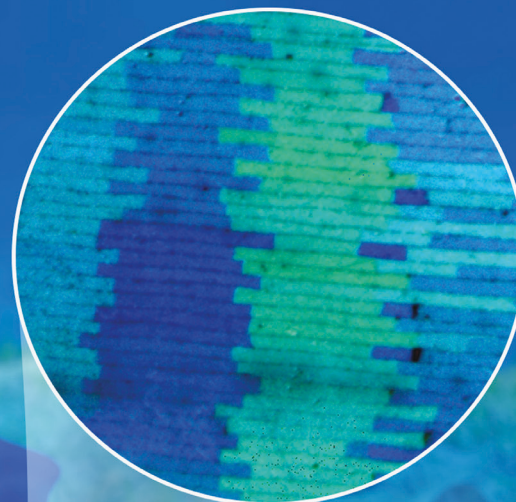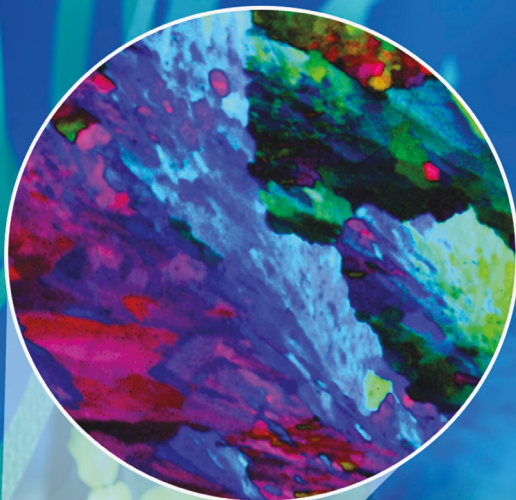et al.

Publication Date
2023-07-01

DOI
10.1002/adma.202300373

Peer reviewed

ADVANCED MATERIALS

A Molecular-Scale Understanding of Misorientation Toughening in Corals and Seashells

Andrew J. Lew, Cayla A. Stifler, Alexandra Tits, Connor A. Schmidt, Andreas Scholl, Astrid Cantamessa, Laura Müller, Yann Delaunois, Philippe Compère, Davide Ruffoni, Markus J. Buehler,* and Pupa U. P. A. Gilbert*

Biominerals are organic–mineral composites formed by living organisms. They are the hardest and toughest tissues in those organisms, are often polycrystalline, and their mesostructure (which includes nano- and micro-scale crystallite size, shape, arrangement, and orientation) can vary dramatically. Marine biominerals may be aragonite, vaterite, or calcite, all calcium carbonate ($CaCO_3$) polymorphs, differing in crystal structure. Unexpectedly, diverse $CaCO_3$ biominerals such as coral skeletons and nacre share a similar characteristic: Adjacent crystals are slightly misoriented. This observation is documented quantitatively at the micro- and nanoscales, using polarization-dependent imaging contrast mapping (PIC mapping), and the slight misorientations are consistently between 1° and 40°. Nanoindentation shows that both polycrystalline biominerals and abiotic synthetic spherulites are tougher than single-crystalline geologic aragonite. Molecular dynamics (MD) simulations of bicrystals at the molecular scale reveal that aragonite, vaterite, and calcite exhibit toughness maxima when the bicrystals are misoriented by 10°, 20°, and 30°, respectively, demonstrating that slight misorientation alone can increase fracture toughness. Slight-misorientation-toughening can be harnessed for synthesis of bioinspired materials that only require one material, are not limited to specific top-down architecture, and are easily achieved by self-assembly of organic molecules (e.g., aspirin, chocolate), polymers, metals, and ceramics well beyond biominerals.

1. Introduction

Biominerals are crystalline composites formed by living organisms,[1–3] providing a source of inspiration for advanced materials synthesis.[4–6] Different animals, such as mollusks, corals, and ascidian tunicates diverged from one another 600–750 million years ago (Ma).[7–9] But the oldest fossils of biominerals for these three phyla are 535, 510, and 270 Ma, respectively.[8,10] Thus, they started making biominerals independently but, surprisingly, they did so similarly: By attachment of amorphous calcium carbonate precursor particles.[9,11] Amorphous precursors were also observed in a variety of other phyla.[6]

The structure of biominerals has not yet been directly compared across these phyla. Thus, it is possible that structural characteristics are common to all three. If this is true, there may be a material-property that makes the selection of the shared structure beneficial to the animal. Alternatively, the shared structure may be an unavoidable and therefore uninteresting consequence of crystal growth, which is

A. J. Lew, M. J. Buehler
Laboratory for Atomistic and Molecular Mechanics (LAMM)
Massachusetts Institute of Technology
77 Massachusetts Ave., Cambridge, MA 02139, USA
E-mail: mbuehler@mit.edu
A. J. Lew
Department of Chemistry
Massachusetts Institute of Technology
77 Massachusetts Ave., Cambridge, MA 02139, USA

The ORCID identification number(s) for the author(s) of this article can be found under https://doi.org/10.1002/adma.202300373.

C. A. Stifler, C. A. Schmidt, P. U. P. A. Gilbert[+]
Department of Physics
University of Wisconsin
Madison, WI 53706, USA
E-mail: pupa@physics.wisc.edu
A. Tits, A. Cantamessa, L. Müller, D. Ruffoni
Mechanics of Biological and Bioinspired Materials Laboratory
Department of Aerospace and Mechanical Engineering
University of Liège
Liège B-4000, Belgium
C. A. Schmidt, P. U. P. A. Gilbert
Department of Chemistry
University of Wisconsin
Madison, WI 53706, USA
A. Scholl
Advanced Light Source
Lawrence Berkeley National Laboratory
Berkeley, CA 94720, USA

[+]Previously publishing as Gelsomina De Stasio

**ADVANCED
SCIENCE NEWS**

www.advancedsciencenews.com

**ADVANCED
MATERIALS**

www.advmat.de

not functionally useful to the forming organism, as proposed by other authors.[12,13] It is therefore worth putting these alternative and contrasting possibilities through rigorous tests.

Previous work using electron backscatter diffraction (EBSD),[14,15] X-ray diffraction,[16,17] and polarization-dependent imaging contrast (PIC) mapping[18] showed that many biominerals exhibit a complex arrangement of crystal units termed crystallites, 10 nm to 10 µm in size,[19] with diverse shapes, spatial arrangements, and crystal misorientations with respect to one another. These features are collectively defined here as mesoscale (10 nm to 10 µm) structure, or simply "mesostructure".[20] Each biomineral has a characteristic mesostructure, distinct from others in different animal phyla or classes.

Biominerals exhibit different structures at different scale, that is, they are hierarchical materials.[5,21] They are frequently tougher than their components, due to the presence of organics and specific nano-, micro-, milli-, and centimeter structures formed under biological control.[22–25] One of the most iconic and most studied biominerals is nacre, or mother-of-pearl, the iridescent inner lining of many mollusk shells.[15,16,25–35] Nacre is much tougher than single-crystalline aragonite, with different values for fracture toughness reported at different length scales.[36–38] Currey pioneered this fertile field, and measured the so-called work of fracture (measured as the area under the stress–strain curve, not as fracture toughness) on macroscopic samples using tensile and three-point bending tests to be 3000× more fracture tough than aragonite alone.[36] Subsequent work, albeit pointing out the limitations of Currey's tests and proposing other, better tests to measure fracture toughness, found unanimously that Currey was right, nacre's toughness is much greater than monolithic aragonite. The quantification of the increase, however, depends on many parameters, including the nacre sample, hydration, experimental tests, fracture mechanics approach, length scales, etc... For example, Sarikaya et al.[37] using linear elastic fracture mechanics reported an 8× increase in toughness. Barthelat et al. found a 30× increase, using the J-integral approach at the millimeter scale and hydrated samples.[38] Using nanoindentation-based assessment of fracture toughness, instead, the reported increase in indentation fracture toughness or damage tolerance of nacre is approximately 2× or 3× greater than monolithic aragonite. This is still a significant increase, but smaller than found at greater scales, where multiple toughening mechanisms and other factors contribute to nacre toughness.[31,33,39]

Because they are scale-dependent, toughness values measured at different scales should not be compared directly. However, in relative terms, if a polycrystalline material exhibits microscale toughness greater than monolithic crystals, the same trend is usually observed and in fact reinforced at greater length scales. A similar trend is observed in other biological materials considered exceptional for their fracture toughness, such as the amorphous silica spicules made by sponges. The indentation-based fracture toughness of the spicules, which have a laminate architecture, is less than 2.5× greater than fused quartz or monolithic spicules.[40] Nevertheless, such microscale increase in material toughness is sufficient to build huge glass spicules at the macroscale, up to 3 m in length and 1 cm in diameter, that anchor the sponge and provide high bending strength.

Here we analyzed several different biomineral mesostructures and synthetic spherulites at multiple scales with a variety of methods. Unprecedentedly, we analyzed them all quantitatively to explore the misorientation of adjacent crystallite pairs at the microscale. For this analysis, we used PIC mapping, which combines surface sensitivity (3–5 nm[41]), spatial resolution (20 nm[18,42,43]), and large-area imaging (10–100 µm[35,44]) and is therefore ideal to include many crystallites in each mesostructure. PIC mapping is not sensitive to a- or b-, only to c-axis orientation, as X-ray absorption spectra vary when rotating the linear polarization of the illuminating soft-X-rays with respect to the c-axis, but not in the ab-plane.[18] Using PIC mapping, we identified a structural feature common to all biominerals analyzed here. We then used a combination of nanoindentation and scanning electron microscopy (SEM) to measure indentation-based toughness at the microscale, and molecular dynamics (MD) simulations to understand the materials property correlated with this common structure at the nanoscale. Specifically, we measured fracture toughness in biogenic, geologic, and synthetic minerals, then, we simulated bicrystals containing a grain boundary, to explore the molecular-scale mechanism that made this structure common to several diverse biominerals.

2. Results

2.1. Slight Misorientation of Adjacent Crystals in Diverse Biominerals and Synthetic Spherulites Quantitatively Measured by Polarization-Dependent Imaging Contrast Mapping

The skeletons of stony corals, the spicules of tunicate ascidians, and the prisms of bivalve mollusk shells provide structural support or shelter to the animal that builds them. These three biominerals are made of one of the three calcium carbonate ($CaCO_3$) polymorphs: aragonite, vaterite, or calcite, respectively. Along with nacre in modern and fossil shells, including sheet and columnar nacre, six mesostructures of representative biominerals from these diverse animals are presented in the PIC maps of **Figure 1**, which were acquired using synchrotron photoemission electron microscopy (PEEM).[45]

In these PIC maps, the color of each nanoscale pixel displays the c-axis direction for the crystal in that pixel, so that the in-plane and off-plane angles are displayed as the color's hue and brightness, respectively.[18] In color bars, the crystal habit and

Y. Delaunois, P. Compère
Laboratory of Functional and Evolutionary Morphology (FOCUS Research Unit) and Center for Applied Research and Education in Microscopy (CAREM)
University of Liège
Liège B-4000, Belgium

P. U. P. A. Gilbert
Departments of Materials Science and Engineering
Geoscience
University of Wisconsin
Madison, WI 53706, USA

P. U. P. A. Gilbert
Chemical Sciences Division
Lawrence Berkeley National Laboratory
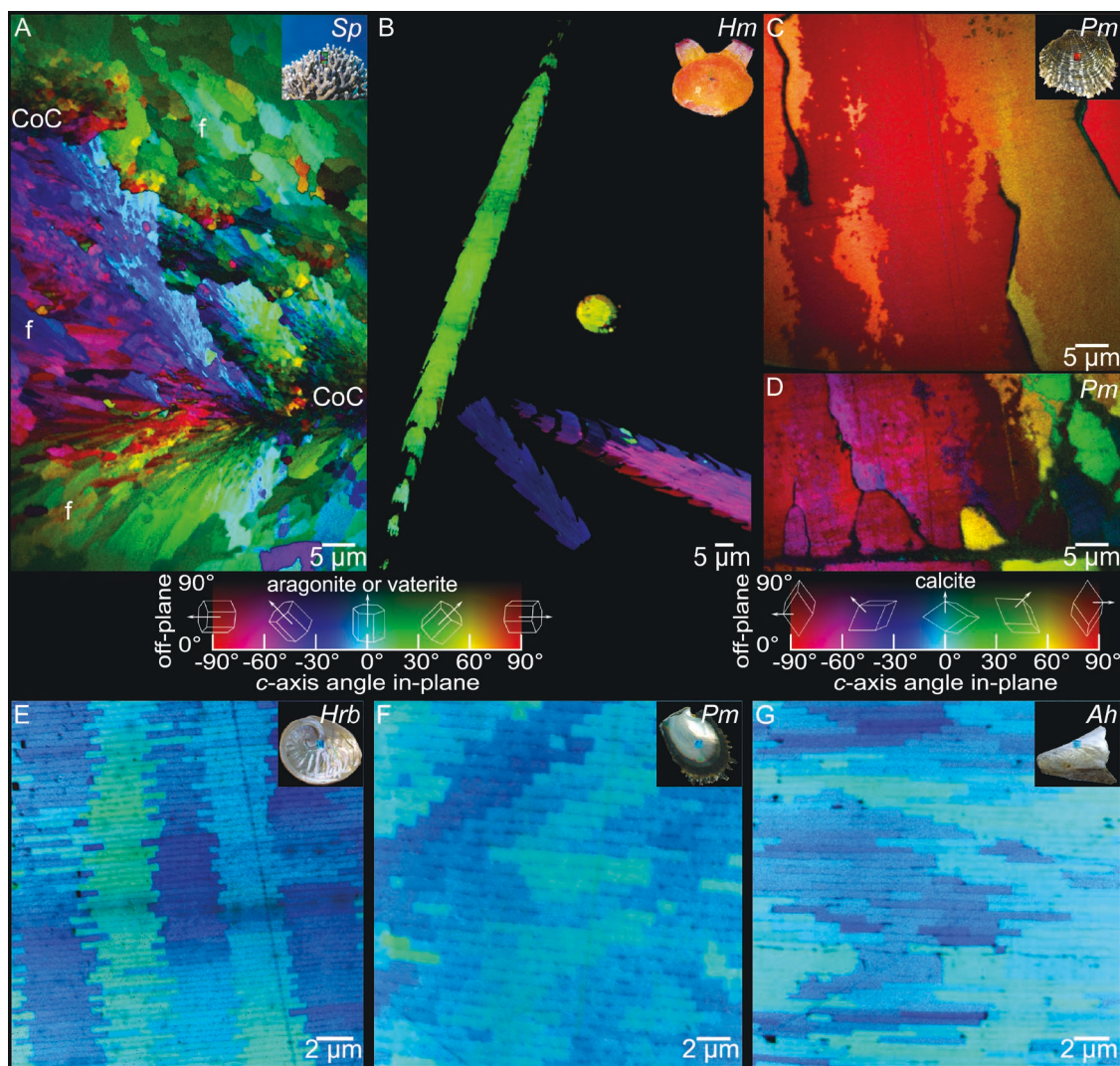Berkeley, CA 94720, USA

Figure 1. Polarization-dependent imaging contrast (PIC) maps display the diverse mesostructures of CaCO₃ biominerals. The orientation of the crystalline *c*-axis is displayed in color, including hue and brightness (see color bars, where schematics indicate crystal habits and *c*-axes) indicating the in-plane and off-plane angles the *c*-axis forms with the polarization plane. All biomineral surfaces are imaged after embedding, polishing, and coating, with the synchrotron beam illuminating at 30° grazing incidence. The approximate position of the PIC map is indicated on the photograph of each biomineral (not to scale). A) Aragonite coral skeleton from *Stylophora pistillata* (*Sp*). Centers of calcification are more nanoparticulate and extend along the non-straight line between "CoC" labels. Acicular fibers "f" form spherulites that radiate from CoCs. B) Vaterite spicules from the tunicate ascidian *Herdmania momus* (*Hm*). C,D) Calcite prisms from the Tahitian pearl oyster *Pinctada margaritifera* (*Pm*). Black pixels are organic envelopes between calcite prisms. Aragonite nacre from three diverse species. E) *Haliotis rubra* (*Hrb*) columnar nacre, characteristic of all nacre-forming gastropods and cephalopods, where cooriented aragonite tablets are stacked into columns, extending perpendicular to the nacre tablet layers. F) *P. margaritifera* (*Pm*) sheet nacre, characteristic of all nacre-forming bivalves, where stacks of cooriented aragonite tablets are staggered diagonally. G) Fossil nacre from a Miocene (13-million-year-old) *Atrina harrisii* (*Ah*). The almost perfectly preserved nacre from this fossil shell is still aragonite and shows diagonally staggered cooriented nacre tablets. Near the bottom of the image, 3–4 nacre layers are fused together, due to diagenesis. All six biomineral mesostructures show at a glance that adjacent crystallites have slight *c*-axis misorientations, as demonstrated by their similar colors in PIC maps. Figure 3 displays these slight misorientations quantitatively.

the *c*-axis direction of each mineral are also shown for additional clarity. The crystal habit is a pseudo-hexagonal prism with the *c*-axis along the prism axis for aragonite or vaterite, or a rhombohedron for calcite, where the c-axis comes out of an obtuse corner of the rhombohedron. Color represents the quantitativelymeasured orientation of the *c*-axis in 3D, which is displayed in 2D images.

Biomineral aragonite can be spherulitic as in coral skeletons (Figure 1A), or lamellar as found in nacre (Figure 1E–G).

Nacre is formed by 3 classes of mollusks: Gastropods, cephalopods, and bivalves. In gastropod and cephalopod nacre, cooriented tablets are organized into straight vertical columns, perpendicular to tablet layers (columnar nacre, Figure 1E), whereas in bivalves cooriented tablets are arranged in diagonally staggered stacks, which may or may not be recognizable in PIC maps depending on how the nacre cutting and polishing plane is oriented compared with the staggering direction (sheet nacre, Figures 1F,G). The structural difference between

**ADVANCED
SCIENCE NEWS**

www.advancedsciencenews.com

**ADVANCED
MATERIALS**

www.advmat.de

sheet and columnar nacre is shown in Figure 1E,F. In both coral spherulite trabeculae and mollusk nacre tablets, adjacent crystals are similarly oriented, as shown by similar colors,[46] adjacent on the color bar. Fossil nacre retains this crystallographic arrangement (Figure 1G).

Biomineral vaterite crystals in spicules formed by tunicate ascidians[47] show a similar result: The left spicule in Figure 1B is mostly green with a few cyan pixels on the lower side of the spicule, the central one in transverse cross-section is green and yellow, the right one is magenta, with spines that are red on one side or blue on the other side, the bottom spicule is mostly dark blue, with dark cyan and dark magenta spines on either side. All of these are adjacent colors on the color bars.

Biomineral calcite in the prismatic outer layer of pinnid bivalve shells is single-crystal-like in each prism of, for example, *Atrina*[48] or *Pinna*,[13] whereas the pteriid bivalve shells such as *Pinctada fucata* and *Pinctada margaritifera* have polycrystalline calcite prisms.[3,17,18,49] The *P. margaritifera* prisms in Figure 1C show the most-commonly observed case with slightly misoriented crystals, all within the red-orange range of colors. Even in the rare prisms with a greater diversity of orientations, such as those in Figure 1D, adjacent crystals have adjacent colors. See also Figures S1–S3, Supporting Information, highlighting adjacent crystals. All crystals in each image were measured, but Figure S3, Supporting Information, shows only a few pairs of adjacent crystals for clarity. A total of 832 pairs of adjacent regions in all samples were analyzed to measure their misorientations.

In all biominerals analyzed here, a key common observation is the slight misorientation of adjacent crystallites in each mesostructure. This slight misorientation is qualitatively visible at a glance in Figure 1: Adjacent crystals always have similar colors. Misorientation was observed before in various biominerals.[3,13–18,24–26,28–30,32–34,42,44,49–57] The nanoscale misorientation of pairs of adjacent crystals, however, was never measured directly and quantitatively, nor compared across diverse biominerals as done here. Note that coral skeletons are formed by so-called plumose spherulites, that is, radial distribution of acicular aragonite crystals starting from a line and radiating in

three dimensions as the fibers in a feather duster or a bottle brush.[42,44] In corals, each of these plumose spherulites is termed "trabecula" and the center line is called centers of calcification, labeled in Figure 1A. Across the boundary between any two trabeculae the orientation is random, thus, abrupt color changes are indeed observed in coral skeletons. These were not included in the misorientation analysis below.

Synthetic aragonite spherical spherulites were also analyzed with PIC mapping and revealed a mesostructure similar to the mesostructure observed within each spherulitic trabecula in coral skeletons. Synthetic spherulites are spherical because radial crystals start from a point, not from a line. A synthetic spherical spherulite is presented in **Figure 2**. In all spherulites, plumose or spherical, adjacent crystals have similar orientations.

Unprecedented and strikingly similar results are presented here in the form of histograms, showing the frequency of each misorientation of the *c*-axes across the boundary between two adjacent crystallites. All misorientations were measured as described in the Supporting Information, and in Figures S1–S3, Supporting Information. In **Figure 3**, no histogram shows misorientations greater than 40°, in any biomineral analyzed here. We subsequently refer to the key 1°–40° misorientation range observed in the histograms of Figure 3 as "slight misorientation," as opposed to larger angles 41° and beyond.

We provide particular attention to nacre, one of the most iconic and well-studied biominerals. It is well-established that adjacent crystalline tablets are slightly misoriented, with *c*-axis misorientation angles within 30° (±15° from the normal to nacre layers).[32,34] These are abiotically selected by a competition for space growth model,[15,28,52] because nacre aragonite grows slowly along the *c*-axis and faster in the *ab*-plane,[28] which is opposite to abiotic aragonite, growing 10× faster along the *c*-axis than along the *a*-axis.[28] Here, we confirm and further refine this observation and find that the misorientation of adjacent tablets in nacre never exceeds 26°, including sheet and columnar nacre, from modern and fossil shells (Figure 3A). This observation is consistent across 6 diverse species of nacre-forming gastropods and bivalves in Figure 3A. This distinctive feature in a material known for its characteristic mechanical
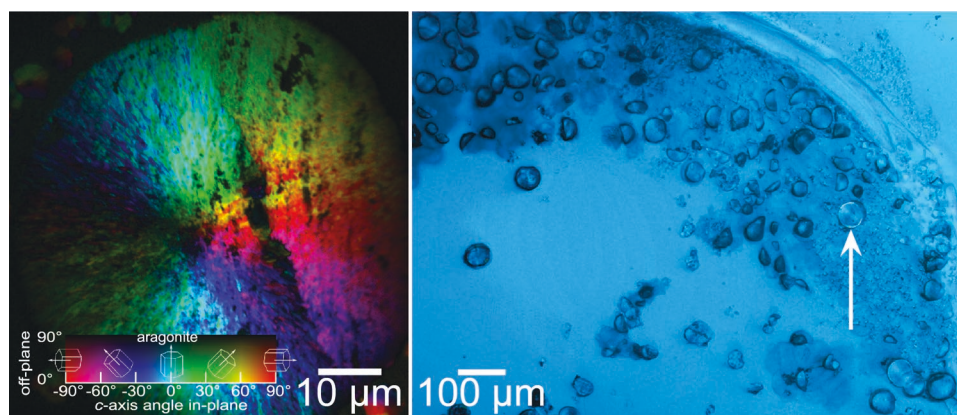

Figure 2. Slight misorientations of adjacent crystals in synthetic aragonite (CaCO₃) spherulites, lacking any organic components. A) PIC map of a spherical aragonite spherulite, grown synthetically in our laboratory. Notice that radial crystals adjacent in space have adjacent colors on the color bar, that is, they are slightly misoriented. B) Polarized light microscopy (PLM) image of many aragonite spherulites, obtained using crossed-polarizers in the illumination and analysis channels. The arrow in (B) indicates the spherulite analyzed with PIC mapping and presented in (A). Each spherulite in (B) is radially banded, as expected in PLM with crossed-polarizers.
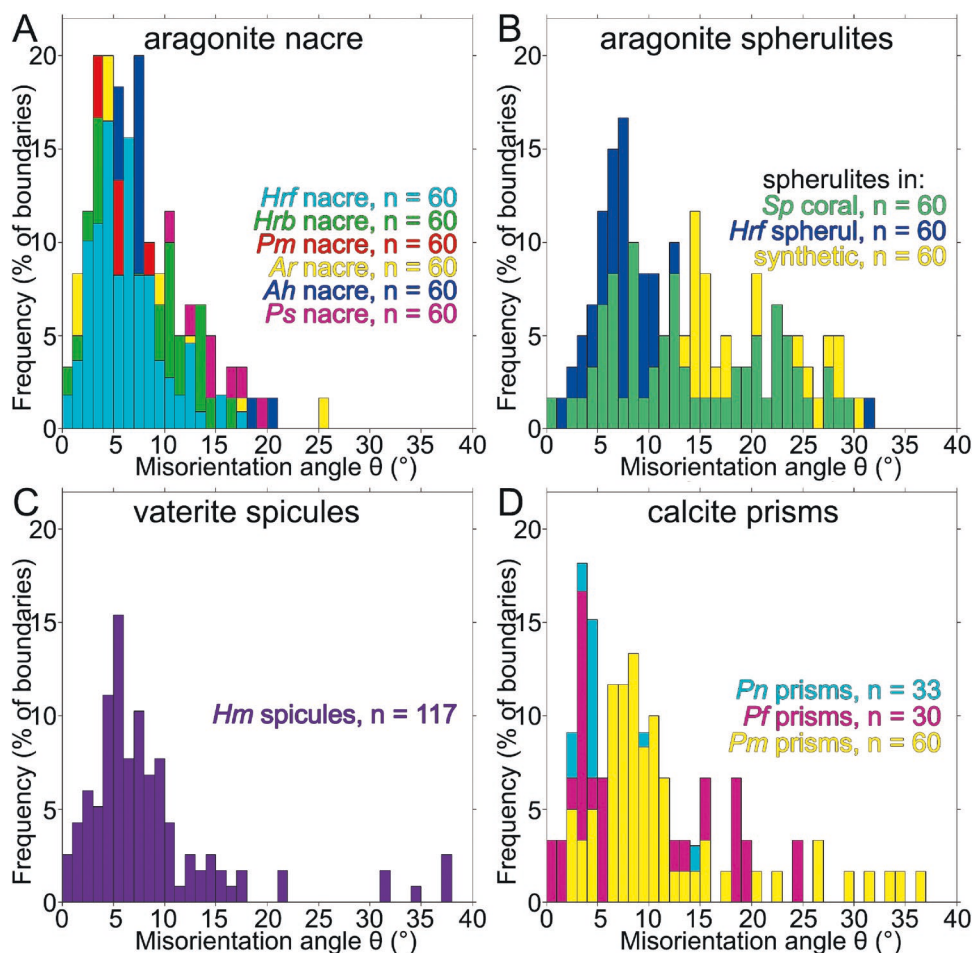
**ADVANCED
SCIENCE NEWS**

www.advancedsciencenews.com

**ADVANCED
MATERIALS**

www.advmat.de

Figure 3. Slight misorientations in CaCO$_3$ biominerals and synthetic spherulites. A) Nacre from 6 different mollusk shells has adjacent tablets with consistently slight misorientation ($\theta < 26°$), making nacre the most ordered of the biominerals studied here. The shells analyzed were from *Haliotis rufescens* (*Hrf*), *H. rubra* (*Hrb*), *Pinctadamargaritifera* (*Pm*), *Atrina rigida* (*Ar*), a 13-million-year-old *A. harrisii* (*Ah*), and a 66-million-year-old *Pinna* sp. (*Ps*). B) Biogenic and synthetic aragonite spherulites have similarly and slightly misoriented adjacent acicular crystallites ($\theta < 35°$). In coral skeletons, from *S. pistillata* (*Sp*), only adjacent crystallites from the same trabecula were selected. Across different trabeculae misorientations were random ($0° < \theta < 90°$). The spherulites in *Hrf* are from the shell shown in Figure 4. C) Vaterite spicules from the ascidian tunicate *H. momus* (*Hm*). D) Calcite prisms from 3 different *Pinctada* species: *P. nigra* (*Pn*), *P. fucata* (*Pf*), and *P. margaritifera* (*Pm*). All these biominerals and synthetic spherulites have $\theta < 40°$. Misorientation, defined as the angular distance between two *c*-axis unit vectors, was measured from pairs of adjacent regions in PIC maps as presented in Figures S1–S3, Supporting Information. Misorientation angles 41°–90° were never found, thus, this angle range is not displayed here. In all histograms, n indicates the number of crystals' pairs measured. Histograms were plotted using MATLAB and overlapped using Adobe Photoshop 2023 for Mac.

toughness[30] provided the first hint at a plausible reason for the prevalence of slight misorientation in biominerals.

Is slight misorientation useful in nacre and all other biominerals? To address this question, we looked at nacre in greater detail, and found a possible answer, after confirming previous observations. As previously observed, at the onset of nacre formation, blocky aragonite crystals seed the orientation of the first tablet crystals at the prismatic-nacre boundary. This was observed in *Pinctada fucata*,[29] *Nautilus pompilius*,[26] and many other mollusk shells,[32] and in red abalone (*Haliotis rufescens*, *Hrf*) a layer of calcite spherulites occasionally grows within nacre, as documented by Zaremba et al.[50] and by Su et al.[58] We confirm that they are not calcite[50] but aragonite.[58] Here, we go far beyond current knowledge by observing that the acicular crystals in these spherulites directly seed the crystal orientations of *Hrf* nacre tablets. **Figure 4** provides direct evidence of this behavior as the growth history of nacre is recorded in

subsequent layers from bottom to top: steady-state nacre is all turquoise, including only cyan, bluish cyan, or greenish cyan in PIC maps (with *c*-axis oriented at −10°, 0°, or +10°, respectively), as seen at the bottom and the top of Figure 4. The layer of spherulites is recognizable by the morphology of spherulites, that is, a semispherical, radial distributions of acicular crystals. Within this spherulitic layer, adjacent crystals in each spherulite are only slightly misoriented, as expected for nearby radii in a sphere, and as observed in all spherulites (geologic, synthetic, biogenic)[42] and in all coral skeletons, including the one in Figure 1A. The spherulitic aragonite crystals directly seed nacre tablet crystal orientations, become layered like nacre, and then, as more misoriented crystals grow more slowly,[28] faster growing crystals with *c*-axes within ±10° (turquoise hues) from the normal to the nacre layers fill space faster and thus prevail over the blue or green crystal orientations. This is evident near the center of Figure 4.
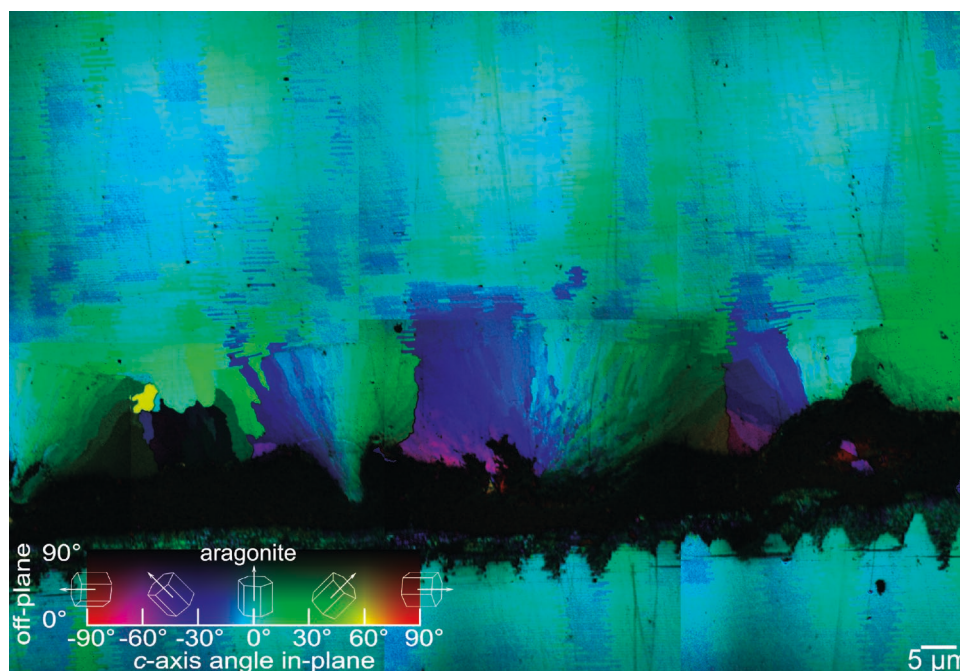
**ADVANCED
SCIENCE NEWS**

www.advancedsciencenews.com

**ADVANCED
MATERIALS**

www.advmat.de

Figure 4. Slight misorientations in nacre start as spherulites. Aragonite nacre from the California red abalone *H. rufescens*. Nacre growth proceeds in the bottom-to-top direction in this cross-section. It is interrupted, an organic dark horizontal layer is formed, then spherulites nucleate, then nacre growth restarts. Notice that the *c*-axis orientations ±10° from the normal to nacre layers (including bluish-cyan, cyan, and greenish-cyan) rapidly prevail as other orientations disappear, such as green, blue, magenta, and yellow in the spherulitic layer and just above it in the first few tens of nacre layers formed epitaxially on spherulites.

Importantly, convergence to steady-state misorientations in nacre seeded by spherulites is faster than at the onset of nacre formation: at the prismatic-nacre (PN) boundary aragonite tablet orientations are random, thus, misorientations reach 90°, and slowly decay to steady state after ≈50 µm from the first nacre layer.[28,32] At the spherulites–nacre (SN) boundary, instead, misorientations reach a maximum of 45°, and rapidly decay to steady state after only ≈20 µm. Figure S4, Supporting Information, shows both results, measured in *Hrf* nacre. This observation suggests that achieving steady-state slight-misorientation faster during shell formation may be useful to the animal, and, therefore, that a materials property may confer that advantage. To explore this suggestion, we used nanoindentation to compare slightly misoriented biominerals and synthetic spherulites to single crystals.

We stress that PIC mapping is not sensitive to azimuthal rotations of the crystal around the *c*-axis, only to polar rotations of the *c*-axis. Thus, only misorientations of *c*-axes were measured and tested by nanoindentation and MD simulations. Azimuthal misorientations, which may very well play a role, remain unexplored and could be investigated in future work.

2.2. Toughness of Slightly Misoriented versus Single-Crystalline Aragonite Crystals, Measured by Nanoindentation

To investigate the relationship between slight misorientation and fracture resistance, we measured the local fracture toughness using nanoindentation. This is an established approach to characterize local fracture behavior of engineering and

biological materials. This method is used here to elucidate the origins of toughness in biominerals by comparing geologic, synthetic, and biogenic aragonites, using the same instrument, conditions, and settings. We followed a procedure widely adopted for biominerals,[23,40,59,60] in which a sharp cube-corner diamond indenter is used to induce cracking at much lower loads than with less sharp standard Berkovich indenter tips. Indents obtained with increasing loads, from mN to N, are then observed by SEM to quantify surface damage. To compare diverse samples, the indentation fracture toughness K_c, was calculated using the following formula:[61]

$$K_c = \chi \left(\frac{E}{H} \right)^{1/2} \left(\frac{P}{c^{3/2}} \right) \tag{1}$$

where χ is a numeric parameter characteristic of the indenter tip geometry ($\chi = 0.04$ for a cube corner), E is the elastic modulus, H is the hardness (measured with nanoindentation at low load/penetration depth and presented in Figure S5, Supporting Information), P is the indentation load, and c is the crack length, measured from the center of the indent.

Single-crystalline geologic aragonite exhibits a typical brittle behavior: radial cracks are already present at lower loads (1–10 mN, Figure S6A, Supporting Information) and increasing the penetration force causes extensive crack propagation along multiple directions (**Figure 5**A). This behavior is consistent with the observed low fracture toughness, that is, $K_c \approx 0.31$ MPa m$^{1/2}$ for geologic aragonite (Figure 5G).

Importantly, we chose to characterize fracture toughness with nanoindentation to probe precisely the same microscale
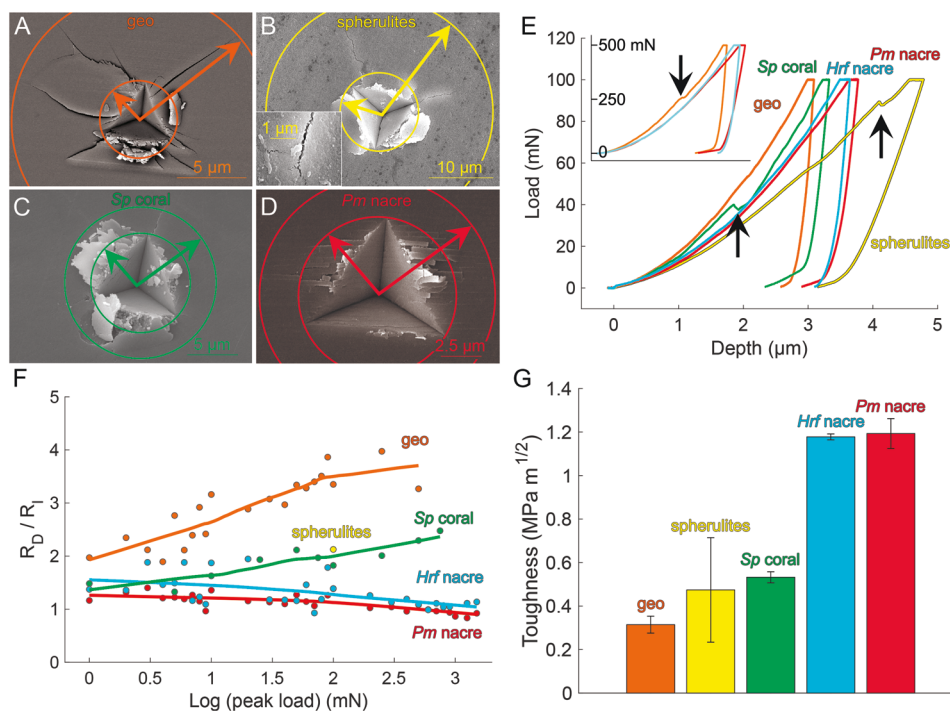
**ADVANCED
SCIENCE NEWS**

www.advancedsciencenews.com

**ADVANCED
MATERIALS**

www.advmat.de

Figure 5. Indentation fracture toughness is greater in aragonite biominerals and synthetic spherulites, compared to single-crystalline geologic aragonite. A–D) SEM images post-indentation with a peak load of 100 mN. In (A), (B), and (D) the indentation direction was perpendicular to the aragonite c-axis, in (C) multiple crystals in coral skeleton have unknown orientations. A) Geologic aragonite crystals indented perpendicular to c-axis, B) synthetic spherulites (inset shows additional toughening mechanisms: crack deflection, microcracking, and crack branching), C) coral skeleton, and D) Pm nacre (indented perpendicular to c-axis, that is, with nacre tablet layers horizontal in the image). Hrf nacre has a behavior qualitatively similar to Pm nacre (Figure S6C, Supporting Information). SEM images are used to extract the radius of the residual indent R_I and of the entire damaged area R_D by fitting the smallest possible circle centered on the indent. E) Typical indentation curves at a peak load of 100 mN: synthetic and coral aragonites show characteristics pop-in events (highlighted by arrows), associated with sudden damage beneath the contact surface. Geologic aragonite also shows such discontinuities but at higher loads, Pm and Hrf nacre do not (see inset), at either lower or higher loads, indicating a progressive damage accumulation but noabrupt pop-in events. F) Ratio of mean damage radius (R_D) and indentation radius (R_I) plotted versus indentation peak load (trend lines are locally weighted scatterplot smoothing, LOWESS, regression fits with a smoothing factor of 0.8). This metric quantifies whether damage tends to localize around the indent (as in Pm and Hrf nacre) or to propagate (as in geo aragonite). Both coral and synthetic spherulites have intermediate behavior. G) Experimentally measured indentation fracture toughness (abbreviated as "Toughness"), obtained by fitting the correlation between damage radius (R_D, a measure of crack length) and indentation load (see Methods in Supporting Information, and Figure S7, Supporting Information).[40,60] Data are presented as mean ± SD over multiple locations within the same sample, except for the spherulites, where 4 different spherulites were measured. Comparison of all the samples demonstrates that slight misorientations, present in synthetic spherulites, coral skeleton, and nacre but absent from geologic aragonite, correspond to greater toughness.

across all the different samples, so the comparison of toughness is possible and quantitatively relevant.

Most interestingly, synthetic spherulites, which have slightly misoriented adjacent crystals but lack any organic interfaces, show a more damage tolerant response, with indents accommodated by both radial cracking and shear induced damage. A closer examination of the damaged surface reveals that the synthetic spherulites are granular, thus, additional toughening mechanisms such as tortuous crack paths, crack deflection, and branching (Figure 5B inset) may also contribute to the observed 50% greater average toughness ($K_c \approx 0.47$ MPa m$^{1/2}$) compared to single-crystalline geologic aragonite.

A similar fracture behavior is observed in coral skeletons: at low to moderate loads (1–25 mN) the contact stress field generates localized pile-up and chipping damage (Figure S6B, Supporting Information). Higher loads are then required to induce radial cracks (Figure 5C and Figure S6B, Supporting Information), which, however, never propagate far from the indent as suggested by the ratio of damage radius R_D to indent size R_I,

which is smaller for coral skeleton than for geologic aragonite (Figure 5F). The corresponding average fracture toughness for coral skeleton is $K_c \approx 0.53$ MPa m$^{1/2}$ (Figure 5G), a 70% increase with respect to geologic single-crystalline aragonite.

Nacre showed the most damage tolerant response: the damage region always remained confined near the indent, as also shown by the ratio of damage to indent radii (Figure 5F) due to multiple toughening mechanisms, including sliding of aragonite tablets, tablet pull out, crack deflection at tablet-tablet boundary in the same layer, within tablets, and at the tablet-organic sheet interface (Figure 5D and Figure S6C,D, Supporting Information). As a result of all these mechanisms combined, nacre has the highest average fracture toughness, with no difference between sheet and columnar nacre ($K_c \approx 1.19$ MPa m$^{1/2}$ and $K_c \approx 1.18$ MPa m$^{1/2}$), in Pm and Hrf nacre, respectively. Nacre shows an almost 300% increase in toughness with respect to geologic aragonite.

Differences in fracture behavior are also reflected in dissimilar indentation curves (Figure 5E): geologic aragonite,

**ADVANCED
SCIENCE NEWS**

www.advancedsciencenews.com

**ADVANCED
MATERIALS**

www.advmat.de

synthetic spherulites, and spherulitic coral skeleton show sudden jumps in the load versus depth curves (arrows in Figure 5E, and inset), which are hallmarks of fracture or sudden damage events beneath the contact point.[2] Such discontinuities are not observed in nacre, even at higher loads, suggesting more gradual damage accumulation and greater damage tolerance.

Comparison of toughness values for all aragonite samples demonstrates that biominerals, including nacre and coral skeletons, are considerably tougher than single crystalline aragonite (Figure 5G). This is consistent with previous studies on geologic and biogenic crystals,[31,33,55,62] identifying the role of organic inclusions and other mechanisms (e.g., friction between rough interfaces and sacrificial mineral bridges) as possible amplifiers for fracture toughness. It is worth mentioning that azimuthal orientation could also influence nanoindentation results. Specifically, changes in the azimuthal angles of the indenter were shown to impact the measured hardness, but not the indentation modulus in both geologic minerals and biominerals.[63] The impact of azimuthal rotations on indentation fracture toughness is not considered here, and it could be explored in future studies. A novel aspect reported here is the fracture behavior of synthetic spherulites: Those structures were grown in the absence of anything organic, and they are on average 50% tougher than geo aragonite. Importantly, the same result is obtained also when indenting aragonite in a different direction with respect to the c-axis (Figure S8, Supporting Information). This observation suggests that, besides structural characteristics such as organic interfaces,[56,64] misorientation of the minerals also contributes to the toughness of $CaCO_3$ biominerals.

2.3. Toughness of Aragonite, Vaterite, Calcite in Molecular Dynamics-Simulated Misoriented Bicrystals, Measured by Mode I Fracture

Indentation experiments indicate that misorientation itself contributes to material toughness, even in the absence of organic components at the interface. However, even when probing synthetic spherulites without organic components, other factors such as shear stresses and material pileup around the indenter likely influence the mechanical measurement. To isolate the effect of misorientation, we next perform MD simulations of $CaCO_3$ bicrystals. We subject these bicrystals to tensile fracture loading and measure toughness as a function of misorientation within each bicrystal. Specifically, the c-axes of the two crystals within each bicrystal are either cooriented ($\theta = 0°$) or misoriented in the range of $\theta = 5°–90°$. The right crystal is notched, and a tensile load is applied vertically to initiate mode I fracture. The crack propagates from right to left, starting from the notch and either continues straight through the material or is deflected by the bicrystal interface. The crystal size, geometry, and loading are illustrated in **Figure 6**A. This geometry was selected because in the case of nacre with horizontal tablet layers, if a crack propagates vertically, it quickly encounters organic sheets and is therefore deflected at those interfaces. In this study we tested crack deflection at the interface of tablets in the same nacre layer, because nacre's tensile strength in the

direction parallel to the tablet layers is far greater than in the normal direction.[51,53] None of the other mechanisms known to toughen nacre[54] are included in these simulations, on purpose, to isolate the specific effects of slight misorientation.

All three $CaCO_3$ polymorphs were investigated, and each simulation was repeated three times to account for slight stochastic differences in fracture propagation. Part of the results are presented in Figure 6B and clearly show greater crack deflection at a slight misorientation angle of 10°, compared to the single crystal (0°). Crack deflection is smaller when the misorientation is increased to a larger 45° angle. Material toughness as a function of misorientation, measured as the integral under the stress–strain curves (Figure S9, Supporting Information), peaks at misorientation angles $\theta = 10°$, 20°, and 30° for aragonite, vaterite, and calcite, respectively, as shown in Figure 6C. Aragonite was additionally subjected to mode I fracture in the normal direction. These cracks simply propagate along the bicrystal interface as expected, independent of misorientation angles, as presented in Figure S10, Supporting Information.

In the case of slight misorientations, increased crack deflection across the interface correlates with increase in toughness. However, at larger angles aragonite exhibits another increase in toughness distinct from the slight misorientation effect. This is likely due to the anisotropic fracture properties of single-crystal aragonite, which has higher toughness when pulled perpendicular ($\gamma = 90°$) to the c-axis than parallel to it ($\gamma = 0°$), as shown in Figure S11B, Supporting Information. Additionally, vaterite single-crystals exhibit secondary fracture from the upper unnotched plane when c-axes are rotated to large angles away from the tensile direction, as shown in Figure S11C, Supporting Information, resulting in crack paths that appear tortuous independent from misorientation toughening. Similarly, calcite single-crystals fail much more readily as their c-axes are rotated away from the tensile direction, with lower yield strains as shown in Figure S11D, Supporting Information, acting as a source of secondary fracture, and providing more tortuous fracture paths without correspondingly high toughness. All three of these large-angle behaviors are due to fracture properties of single-crystals, not to large misorientations of bicrystals.

Despite the above, polymorph-specific, single-crystal behaviors, the common trend in Figure 6 is clear: Slight misorientation makes bicrystals tougher. Specifically, direct comparison of the MD results precisely illustrates the multiplicative effect of slight misorientation on toughness. Misoriented bicrystals of aragonite, vaterite, and calcite become 2.5, 2, and 3 times tougher, respectively, than their cooriented crystal structures. This comparison is presented in Figure S12, Supporting Information, which includes the literature result obtained for hydroxyapatite in human enamel using similar MD simulations.[65]

3. Discussion

The comparison of biomineral mesostructures presented in Figure 1 yields surprising insights, because it reveals that, despite wildly different mesostructures, adjacent crystals have
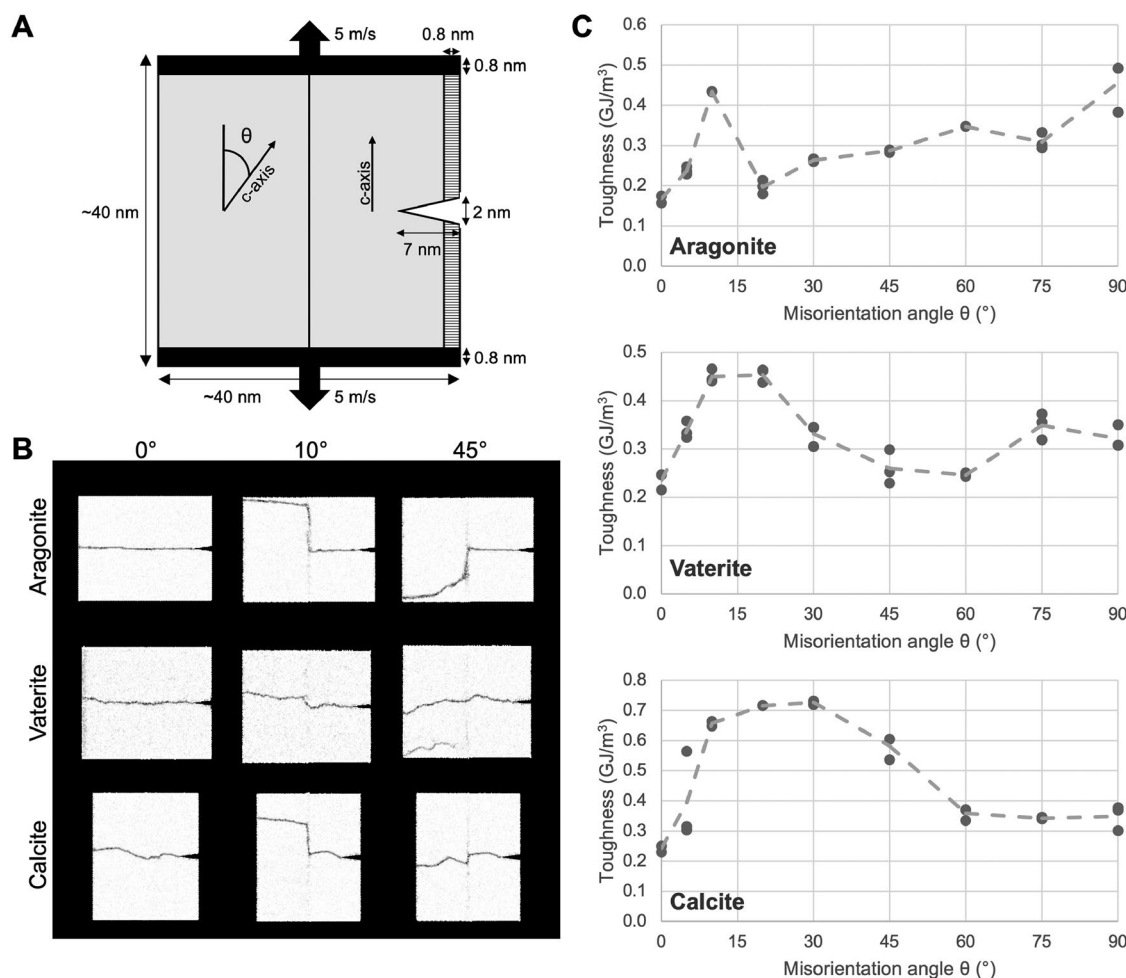
Figure 6. Slight misorientation toughens nacre, when cracks propagate through tablets parallel to nacre layers in MD simulations. A) Aragonite, vaterite, and calcite were subject to mode I fracture. Bicrystal structures were designed to resemble two adjacent nacre tablets in the same nacre layer, and the interface between them. The right crystal c-axis parallel to the tensile direction and vertical and the left crystal c-axis rotated in the plane of the figure by a misorientation angle θ. B) The introduction of a misoriented interface results in qualitative crack deflection, with a larger effect at 10° than 45°. C) Fracture toughness calculated across a range of misorientations quantitatively shows that toughness has a peak at small angles: Approximately 10°, 20°, and 30° for aragonite, vaterite, and calcite, respectively. Each simulation was repeated 3 times.

similar colors, that is, are slightly misoriented at the micro- and nanoscales.

No two biomineral mesostructures could have more diverse morphologies than nacre, with tablets arranged as brick-and-mortar, and coral skeletons, with acicular fibers arranged in spherulites. Yet, from the point of view of slight misorientation of adjacent crystals, nacre and corals skeletons are quite similar. One could even say that nacre is spherulitic. In fact, nacre can start spherulitic, as shown in Figure 4, and then slight misorientations are selected abiotically, by competition for space. If one accepts that slight misorientations are better than larger ones, then faster convergence to steady-state-nacre misorientations of 20° within 20 μm, instead of the usual 50 μm observed at the prismatic-nacre boundary,[28,32] makes nacre tougher faster, limits the volume of lower-toughness nacre, thus, it makes the overall nacre layer and its mesolayers[51] more durable. It is unclear at present how much a thinner greater misorientation layer makes the overall material tougher. As an aside, many blocky, equant, aragonite crystals in the

literature were incorrectly termed spherulitic by other groups and ours,[28] because they are equant and single-crystalline, but they are not a distribution of acicular crystals, slightly and gradually changing in orientation like the spherulites in Figures 1A and 2. Spherulitic aragonite, forming after an organic layer in *Hrf* nacre,[58] seeds the orientation of nacre tablets as shown in the PIC map of Figure 4. This map includes both spherulites and nacre tablets and shows that cyan acicular crystals in spherulites become layered nacre tablets with the same color and orientation. Thus, biominerals that may seem completely distinct under a traditional lens may share features after all.

Indeed, the observation that diverse biominerals share slight misorientations suggests that these could provide an evolutionary advantage. Nanoindentation experiments on biominerals and synthetic spherulites indicated that slight misorientation is, among other factors, a potential toughening mechanism. However, neither experiment could prove direct correlation of toughness and slight misorientation, because the systems are too complex and feature many toughening

**ADVANCED
SCIENCE NEWS**

www.advancedsciencenews.com

**ADVANCED
MATERIALS**

www.advmat.de

strategies all occurring simultaneously, making it impossible to isolate misorientation for a direct comparison. Therefore, we employed MD simulations to isolate the effect of the misorientation in a controlled bicrystal system, and determine a clear relationship between slight misorientations and toughening in bicrystals. No parameters other than misorientation angles were varied, thus, the results of MD experiments are clear: slight misorientations of 10°, 20°, 30° in aragonite, vaterite, and calcite, respectively, most effectively toughen bicrystals.

Importantly, nanoindentation at the microscale and MD simulations at the nanoscale are two independent methods of obtaining toughness trends and, although these are not directly and quantitatively comparable to one another, they agree with one another about greater toughness at slight misorientation angles. The measured microscale toughness results are in good agreement with previous data at the same scale.[31,33,39]

We stress that MD simulations were done on the simplest possible system, including only two sintered crystals and the interface between them. They do not contain any hierarchical structure that could contribute to toughness, or any additional materials at the interface, which could also toughen. These additional features, ubiquitous in natural biominerals, were omitted on purpose to test the effect of crystal misorientation alone, not in combination with other mechanisms.

Azimuthal misorientations of adjacent crystallites may also play a role in toughening biominerals, but those remain unexplored. Future studies could detect such misorientations using EBSD, accompanied by nanoindentation or MD simulations, to explore that additional effect.

In previous studies, remarkable improvements in materials properties were observed with low-angle and high-angle grain boundaries in metals and superconductors.[66] The separation between the two regimes was always 15°.[67] The misorientations of adjacent crystals observed in natural biominerals and synthetic spherulites do not fit squarely into either category. They are indeed observed at grain boundaries, but they are not segregated along the same low-angle (<15°) or high-angle (>15°) criteria. Instead, PIC mapping experiments confirm that the observed misorientations peak at approximately 5°–15° but they include many other angles between 1° and 40°, albeit less frequently (see Figure 3 histograms). Thus, a new category must be added: slight misorientation, $1° < \theta < 40°$, as presented here.

Furthermore, MD simulations were done at the nanoscale whereas misorientation and nanoindentation-toughness were measured at the microscale. Performing these measurements at the same scale is challenging at present and could not be done here.

Can an organism benefit at the macroscale from the micro- or molecular-scale toughening observed here? If the aforementioned example of sponge spicules is a guide, then the answer may be yes, and in fact the macroscale toughness may build upon the molecular-scale toughness, at the micro- and macroscales, and thus significantly increase toughness with scale.

Because increasing values of fracture toughness were measured at increasing length scales in hierarchical heterogeneous composites such as nacre (see introduction), here we chose to explore fracture toughness at the smallest possible scales: the microscale with indentation and the molecular scale using MD simulations. At the molecular scale, MD simulations reveal the

Table 1. Comparison of MD-predicted misorientation toughness maxima and observed misorientation angles.

Mineral	Maximum toughness in MD simulations	Most frequently observed misorientation angle
Aragonite	10°	5° in nacre
Aragonite	10°	5° in shell spherulites
Aragonite	10°	15° in coral skeletons
Vaterite	10°–20°	5° in tunicate spicules
Calcite	20°–30°	5°–10° in *Pinctada* prisms

direct relationships between crystal orientations and toughness to a level inaccessible by experiment alone.

Many toughening mechanisms have been observed in biological materials.[24,68] Even slight misorientation of adjacent crystals was recently observed in human enamel and shown, with MD simulations similar to those presented here, to be functional in preventing fracture.[65] Now the present work recontextualizes this enamel observation as a piece of a larger view that slight misorientation toughening is a more general mechanism across many biominerals. The fact that enamel is so different in mineralogy and mesostructure from $CaCO_3$ biominerals further supports the idea that slight misorientations toughen biominerals, and it may therefore provide evolutionary advantages to the forming organisms.

Comparing the maxima predicted by MD simulations for aragonite, vaterite, and calcite, respectively, they do not correspond precisely to the angles most frequently observed in the biogenic and synthetic systems, as shown in **Table 1**.

The values in Table 1 do not correspond precisely. For both MD-simulation and PIC mapping experiments, however, the maxima occur at angles below 30°–40°. Future work by the bio-inspired materials synthesis community will be necessary to fully harness the slight misorientation-toughening observed here, and to predict the parameters that can best control it.

4. Conclusions

We have compared biomineral structures and surprisingly found that diverse organisms make their biominerals with adjacent crystals similarly slightly misoriented. MD simulations and nanoindentation experiments concur with one another on this observation, albeit with slight numeric differences. This observation in natural biominerals suggests that synthetic materials could be made tougher by small misorientations. The latter is expected to be relatively simple, because many synthetic, geologic, or biogenic crystals spontaneously grow spherulitically,[42,44] that is, as needle-like crystals radiating from common centers, and, in all spherulites, adjacent crystals are always slightly misoriented, and therefore tough. A key advantage of the bioinspired slight-misorientation-tough spherulitic structure is that it only requires one, not multiple materials with a specific architecture templating another in a top-down approach. It can be easily achieved by self-assembly of organic molecules such as aspirin[69] and cocoa butter in chocolate,[70] polymers,[71] graphite in cast iron,[72] semiconductors,[73] and many more systems, well beyond calcium carbonate

ADVANCED
SCIENCE NEWS
www.advancedsciencenews.com

ADVANCED
MATERIALS
www.advmat.de

biominerals. Thus, the observation of slight-misorientation-toughening in this work is relevant to stimulate the synthesis of bioinspired materials with useful functions and enhanced toughness.

5. Experimental Section

Detailed materials and methods are provided in Supporting Information.

Supporting Information

Supporting Information is available from the Wiley Online Library or from the author.

Conflict of Interest

The authors declare no conflict of interest.

Author Contributions

P.U.P.A.G. conceived the idea that slight misorientation is similar across biominerals for a materials reason, and that MD simulations could be used to test this idea. M.J.B. and A.J.L. designed the MD simulations and fracture analyses, and A.J.L. carried out the molecular-scale simulations, collected the data, and visualized the results. The simulations were analyzed and interpreted (in conjunction with the experimental data) by A.J.L., M.J.B., and P.U.P.A.G. C.A.Sc., C.A.St., A.S., and P.U.P.A.G. acquired all the PIC mapping data. D.R. designed the nanoindentation experiments and SEM analysis. A.T., A.C., L.M., and D.R. acquired and processed all nanoindentation data. L.M., P.C., and Y.D. performed SEM and A.T., A.C., and L.M. analyzed post-indentation images. Nanoindentation and SEM data were interpreted by A.T., A.C., L.M., D.R., and P.U.P.A.G. C.A.Sc. prepared the synthetic spherulites. C.A.St. and P.U.P.A.G. collected and processed all the misorientation data for the histograms in Figure 3. P.U.P.A.G. prepared Figures 1–4, A.T., A.C., L.M., and D.R. prepared Figure 5, A.J.L. prepared Figure 6. P.U.P.A.G. wrote the manuscript, all co-authors edited it.

Data Availability Statement

The data that support the findings of this study are available from the corresponding author upon reasonable request.

[1] a) W. J. Shaw, J. R. Long, A. A. Campbell, P. S. Stayton, G. P. Drobny, *J. Am. Chem. Soc.* **2000**, *122*, 7118; b) J. Aizenberg, A. Tkachenko, S. Weiner, L. Addadi, G. Hendler, *Nature* **2001**, *412*, 819; c) L. Addadi, S. Raz, S. Weiner, *Adv. Mater.* **2003**, *15*, 959; d) J. Aizenberg, J. C. Weaver, M. S. Thanawala, V. C. Sundar, D. E. Morse, P. Fratzl, *Science* **2005**, *309*, 275; e) L. Addadi, D. Joester, F. Nudelman, S. Weiner, *Chemistry* **2006**, *12*, 980; f) Y. Politi, R. A. Metzler, M. Abrecht, B. Gilbert, F. H. Wilt, I. Sagi, L. Addadi, S. Weiner, P. U. P. A. Gilbert, *Proc. Natl. Acad. Sci. USA* **2008**, *105*, 17362; g) Y. U. T. Gong, C. E. Killian, I. C. Olson, N. P. Appathurai, A. L. Amasino, M. C. Martin, L. J. Holt, F. H. Wilt, P. U. P. A. Gilbert, *Proc. Natl. Acad. Sci. USA* **2012**, *109*, 6088; h) J. C. Weaver, G. W. Milliron, A. Miserez, K. Evans-Lutterodt, S. Herrera, I. Gallana, W. J. Mershon, B. Swanson, P. Zavattieri, E. DiMasi, *Science* **2012**, *336*, 1275; i) B. Bayerlein, P. Zaslansky, Y. Dauphin, A. Rack, P. Fratzl, I. Zlotnikov, *Nat. Mater.* **2014**, *13*, 1102; j) O. Branson, E. A. Bonnin, D. E. Perea, H. J. Spero, Z. Zhu, M. Winters, B. Hönisch, A. D. Russell, J. S. Fehrenbacher, A. C. Gagnon, *Proc. Natl. Acad. Sci. USA* **2016**, *113*, 12934; k) T. Mass, A. J. Giuffre, C.-Y. Sun, C. A. Stifler, M. J. Frazier, M. Neder, N. Tamura, C. V. Stan, M. A. Marcus, P. U. P. A. Gilbert, *Proc. Natl. Acad. Sci. USA* **2017**, *114*, E7670; l) C. A. Schmidt, C. A. Stifler, E. L. Luffey, B. I. Fordyce, A. Ahmed, G. B. Pujol, C. P. Breit, S. S. Davison, C. N. Klaus, I. J. Koehler, I. M. LeCloux, C. M. Diaz, C. M. Nguyen, V. Quach, J. S. Sengkhammee, E. J. Walch, M. M. Xiong, E. Tambutté, S. Tambutté, T. Mass, P. U. P. A. Gilbert, *J. Am. Chem. Soc.* **2022**, *144*, 1332; m) T. Yang, H. Chen, Z. Jia, Z. Deng, L. Chen, E. M. Peterman, J. C. Weaver, L. Li, *Science* **2022**, *375*, 647.

[2] S. Amini, M. Tadayon, S. Idapalapati, A. Miserez, *Nat. Mater.* **2015**, *14*, 943.

[3] F. Mastropietro, P. Godard, M. Burghammer, C. Chevallard, J. Daillant, J. Duboisset, P. Allain, P. Guenoun, J. Nouet, V. Chamard, *Nat. Mater.* **2017**, *16*, 946.

[4] a) V. Schoeppler, P. K. Cook, C. Detlefs, R. Demichelis, I. Zlotnikov, *Adv. Mater.* **2022**, *34*, 2200690; b) C. Tang, Y. Wei, L. Gu, Q. Zhang, M. Li, G. Yuan, Y. He, L. Huang, Y. Liu, Y. Zhang, *Adv. Sci.* **2020**, *7*, 1902536; c) F. C. Meldrum, C. O'Shaughnessy, *Adv. Mater.* **2020**,

32, 2001068; d) W. Huang, D. Restrepo, J. Y. Jung, F. Y. Su, Z. Liu, R. O. Ritchie, J. McKittrick, P. Zavattieri, D. Kisailus, *Adv. Mater.* **2019**, *31*, 1901561; e) E. Seknazi, B. Pokroy, *Adv. Mater.* **2018**, *30*, 1707263; f) S. Yao, B. Jin, Z. Liu, C. Shao, R. Zhao, X. Wang, R. Tang, *Adv. Mater.* **2017**, *29*, 1605903; g) G. Zan, Q. Wu, *Adv. Mater.* **2016**, *28*, 2099; h) A. Gal, V. Brumfeld, S. Weiner, L. Addadi, D. Oron, *Adv. Mater.* **2012**, *24*, OP77; i) R. Q. Song, H. Cölfen, *Adv. Mater.* **2010**, *22*, 1301; j) Y. Y. Kim, L. Ribeiro, F. Maillot, O. Ward, S. J. Eichhorn, F. C. Meldrum, *Adv. Mater.* **2010**, *22*, 2082; k) J. Aizenberg, *Adv. Mater.* **2004**, *16*, 1295; l) E. Dujardin, S. Mann, *Adv. Mater.* **2002**, *14*, 775; m) S. Raz, S. Weiner, L. Addadi, *Adv. Mater.* **2000**, *12*, 38.

[5] a) A. S. Schenk, I. Zlotnikov, B. Pokroy, N. Gierlinger, A. Masic, P. Zaslansky, A. N. Fitch, O. Paris, T. H. Metzger, H. Cölfen, *Adv. Funct. Mater.* **2012**, *22*, 4668; b) F. Nudelman, N. A. Sommerdijk, *Angew. Chem., Int. Ed.* **2012**, *51*, 6582.

[6] L. Addadi, S. Raz, S. Weiner, *Adv. Mater.* **2003**, *15*, 959.

[7] A. H. Knoll, in *Biomineralization and Evolutionary History*, Reviews in Mineralogy & Geochemistry, Vol. *54* (Eds: P. M. Dove, J. J. De Yoreo, S. Weiner), de Gruyter/Mineralogical Society of America, Washington, DC **2003**, pp. 329–355.

[8] P. U. P. A. Gilbert, K. D. Bergmann, N. Boekelheide, S. Tambutté, T. Mass, F. Marin, J. Adkins, J. Erez, B. Gilbert, V. Knutson, M. Cantine, J. O. Henrandez, A. H. Knoll, *Sci. Adv.* **2022**, *8*, eabl9653.

[9] P. U. P. A. Gilbert, S. M. Porter, C.-Y. Sun, S. Xiao, B. M. Gibson, N. Shenkar, A. H. Knoll, *Proc. Natl. Acad. Sci. USA* **2019**, *116*, 17659.

[10] a) A. Kouchinsky, S. Bengtson, B. Runnegar, C. Skovsted, M. Steiner, M. Vendrasco, *Geol. Mag.* **2012**, *149*, 221; b) A. C. Maloof, S. M. Porter, J. L. Moore, F. Dudás, S. A. Bowring, J. A. Higgins, D. A. Fike, M. P. Eddy, *Geol. Soc. Am. Bull.* **2010**, *122*, 1731; c) J. Wendt, *Palaeontology* **2018**, *61*, 575.

[11] J. J. De Yoreo, P. U. P. A. Gilbert, N. A. J. M. Sommerdijk, R. L. Penn, S. Whitelam, D. Joester, H. Zhang, J. D. Rimer, A. Navrotsky, J. F. Banfield, A. F. Wallace, F. M. Michel, F. C. Meldrum, H. Cölfen, P. M. Dove, *Science* **2015**, *349*, aaa6760.

[12] A. Seilacher, *Syst. Zool.* **1973**, *22*, 451.

[13] V. Schoeppler, D. Stier, R. J. Best, C. Song, J. Turner, B. H. Savitzky, C. Ophus, M. A. Marcus, S. Zhao, K. Bustillo, *Adv. Mater.* **2021**, *33*, 2101358.

[14] a) S. C. Fitzer, V. R. Phoenix, M. Cusack, N. A. Kamenos, *Sci. Rep.* **2014**, *4*, 6218; b) X. Yin, E. Griesshaber, A. Checa, F. Nindiyasari-Behal, I. Sánchez-Almazo, A. Ziegler, W. Schmahl, *J. Struct. Biol.* **2021**, *213*, 107707.

[15] A. G. Checa, T. Okamoto, J. Ramírez, *Proc. R. Soc. B: Biol. Sci.* **2006**, *273*, 1329.

[16] A. G. Checa, A. B. Rodríguez-Navarro, *Biomaterials* **2005**, *26*, 1071.

[17] I. C. Olson, R. A. Metzler, N. Tamura, M. Kunz, C. E. Killian, P. U. P. A. Gilbert, *J. Struct. Biol.* **2013**, *183*, 180.

[18] P. U. P. A. Gilbert, A. Young, S. N. Coppersmith, *Proc. Natl. Acad. Sci. USA* **2011**, *108*, 11350.

[19] R. Q. Song, H. Cölfen, *Adv. Mater.* **2010**, *22*, 1301.

[20] P. U. P. A. Gilbert, *MRS Bull.* **2023**, https://doi.org/10.1557/s43577-023-00479-7.

[21] a) J. D. Currey, *Science* **2005**, *309*, 253; b) P. Simon, D. Zahn, H. Lichte, R. Kniep, *Angew. Chem., Int. Ed.* **2006**, *45*, 1911; c) R. Przeniosło, J. Stolarski, M. Mazur, M. Brunelli, *J. Struct. Biol.* **2008**, *161*, 74; d) H. Imai, Y. Oaki, *MRS Bull.* **2010**, *35*, 138; e) E. Beniash, *Wiley Interdisc. Rev.: Nanomed. Nanobiotechnol.* **2011**, *3*, 47.

[22] S. Kamat, X. Su, R. Ballarini, A. Heuer, *Nature* **2000**, *405*, 1036.

[23] M. A. Marcus, S. Amini, C. A. Stifler, C.-Y. Sun, M. J. Frazier, N. Tamura, H. A. Bechtel, D. Y. Parkinson, H. S. Barnard, X. X. X. Zhang, J. Q. I. Chua, A. Miserez, P. U. P. A. Gilbert, *ACS Nano* **2017**, *11*, 11856.

[24] W. Huang, D. Restrepo, J. Y. Jung, F. Y. Su, Z. Liu, R. O. Ritchie, J. McKittrick, P. Zavattieri, D. Kisailus, *Adv. Mater.* **2019**, *31*, 1901561.

[25] H.-C. Loh, T. Divoux, B. Gludovatz, P. U. Gilbert, R. O. Ritchie, F.-J. Ulm, A. Masic, *Commun. Mater.* **2020**, *1*, 77.

[26] H. Mutvei, *Biomineralization* **1972**, *4*, 81.

[27] a) B. Bruet, H. Qi, M. Boyce, R. Panas, K. Tai, L. Frick, C. Ortiz, *J. Mater. Res.* **2005**, *20*, 2400; b) M. A. Meyers, A. Y.-M. Lin, P.-Y. Chen, J. Muyco, *J. Mech. Behav. Biomed. Mater.* **2008**, *1*, 76; c) R. A. Metzler, J. S. Evans, C. E. Killian, D. Zhou, T. H. Churchill, N. P. Appathurai, S. N. Coppersmith, P. U. P. A. Gilbert, *J. Am. Chem. Soc.* **2010**, *132*, 6329; d) I. C. Olson, R. Kozdon, J. W. Valley, P. U. P. A. Gilbert, *J. Am. Chem. Soc.* **2012**, *134*, 7351; e) R. T. DeVol, C.-Y. Sun, M. A. Marcus, S. N. Coppersmith, S. C. B. Myneni, P. U. P. A. Gilbert, *J. Am. Chem. Soc.* **2015**, *137*, 13325.

[28] P. U. P. A. Gilbert, R. A. Metzler, D. Zhou, A. Scholl, A. Doran, A. Young, M. Kunz, N. Tamura, S. N. Coppersmith, *J. Am. Chem. Soc.* **2008**, *130*, 17519.

[29] K. Saruwatari, T. Matsui, H. Mukai, H. Nagasawa, T. Kogure, *Biomaterials* **2009**, *30*, 3028.

[30] F. Barthelat, *Bioinspiration Biomimetics* **2010**, *5*, 035001.

[31] Z. Huang, X. Li, *Sci. Rep.* **2013**, *3*, 1693.

[32] I. C. Olson, A. Z. Blonsky, N. Tamura, M. Kunz, P. U. P. A. Gilbert, *J. Struct. Biol.* **2013**, *184*, 454.

[33] S. Wang, X. Zhu, Q. Li, R. Wang, X. Wang, *J. Struct. Biol.* **2016**, *194*, 199.

[34] P. U. P. A. Gilbert, K. D. Bergmann, C. E. Myers, M. A. Marcus, R. T. DeVol, C.-Y. Sun, A. Z. Blonsky, E. Tamre, J. Zhao, E. A. Karan, N. Tamura, S. Lemer, A. J. Giuffre, G. Giribet, J. M. Eiler, A. H. Knoll, *Earth Planet. Sci. Lett.* **2017**, *460*, 281.

[35] R. T. DeVol, R. A. Metzler, L. Kabalah-Amitai, B. Pokroy, Y. Politi, A. Gal, L. Addadi, S. Weiner, A. Fernandez-Martinez, R. Demichelis, J. D. Gale, J. Ihli, F. C. Meldrum, A. Z. Blonsky, C. E. Killian, C. B. Salling, A. T. Young, M. A. Marcus, A. Scholl, A. Doran, C. Jenkins, H. A. Bechtel, P. U. P. A. Gilbert, *J. Phys. Chem. B* **2014**, *118*, 8449.

[36] J. D. Currey, *Procs. R Soc. B: Biol. Sci.* **1977**, *196*, 443.

[37] M. Sarikaya, K. Gunnison, M. Yasrebi, I. Aksay, *MRS Online Proc. Libr.* **1990**, *174*, 109.

[38] F. Barthelat, H. Espinosa, *Exp. Mech.* **2007**, *47*, 311.

[39] Z. Deng, L. Li, unpublished.

[40] A. Miserez, J. C. Weaver, P. J. Thurner, J. Aizenberg, Y. Dauphin, P. Fratzl, D. E. Morse, F. W. Zok, *Adv. Funct. Mater.* **2008**, *18*, 1241.

[41] P. U. P. A. Gilbert, in *Biomineralization Sourcebook, Characterization of Biominerals and Biomimetic Materials* (Eds: E. DiMasi, L. B. Gower), CRC Press, Boca Raton, FL, USA **2014**, p. 135.

[42] C.-Y. Sun, M. A. Marcus, M. J. Frazier, A. J. Giuffre, T. Mass, P. U. Gilbert, *ACS Nano* **2017**, *11*, 6612.

[43] G. De Stasio, L. Perfetti, B. Gilbert, O. Fauchoux, M. Capozi, P. Perfetti, G. Margaritondo, B. P. Tonner, *Rev. Sci. Instrum.* **1999**, *70*, 1740.

[44] C.-Y. Sun, L. Gránásy, C. A. Stifler, T. Zaquin, R. V. Chopdekar, N. Tamura, J. C. Weaver, J. A. Y. Zhang, S. Goffredo, G. Falini, M. A. Marcus, T. Pusztai, V. Schoeppler, T. Mass, P. U. P. A. Gilbert, *Acta Biomater.* **2021**, *120*, 277.

[45] a) G. De Stasio, M. Capozi, G. F. Lorusso, P. A. Baudat, T. C. Droubay, P. Perfetti, G. Margaritondo, B. P. Tonner, *Rev. Sci. Instrum.* **1998**, *69*, 2062; b) B. H. Frazer, M. Girasole, L. M. Wiese, T. Franz, G. De Stasio, *Ultramicroscopy* **2004**, *99*, 87; c) J. Feng, A. Scholl, in *Science of Microscopy* (Eds: P. W. Hawkes, J. C. H. Spence, J. Feng, A. Scholl), Springer, New York **2007**, pp. 657–695.

[46] P. U. P. A. Gilbert, *Physics in the Arts*, Academic Press, Cambridge, MA, USA **2021**.

[47] a) H. A. Lowenstam, D. P. Abbott, *Science* **1975**, *188*, 363; b) B. Pokroy, L. Kabalah-Amitai, I. Polishchuk, R. T. DeVol,

**ADVANCED
SCIENCE NEWS**

www.advancedsciencenews.com

**ADVANCED
MATERIALS**

www.advmat.de

A. Z. Blonsky, C.-Y. Sun, M. A. Marcus, A. Scholl, P. U. Gilbert, *Chem. Mater.* **2015**, *27*, 6516; c) L. Kabalah-Amitai, B. Mayzel, Y. Kauffmann, A. N. Fitch, L. Bloch, P. U. Gilbert, B. Pokroy, *Science* **2013**, *340*, 454.

[48] H. Li, H. L. Xin, M. E. Kunitake, E. C. Keene, D. A. Muller, L. A. Estroff, *Adv. Funct. Mater.* **2011**, *21*, 2028.

[49] A. G. Checa, J. T. Bonarski, M. G. Willinger, M. Faryna, K. Berent, B. Kania, A. González-Segura, C. M. Pina, J. Pospiech, A. Morawiec, *J. R. Soc. Interface* **2013**, *10*, 20130425.

[50] C. M. Zaremba, A. M. Belcher, M. Fritz, Y. Li, S. Mann, P. K. Hansma, D. E. Morse, J. S. Speck, G. D. Stucky, *Chem. Mater.* **1996**, *8*, 679.

[51] A. Lin, M. A. Meyers, *Mater. Sci. Eng. A* **2005**, *390*, 27.

[52] R. A. Metzler, D. Zhou, M. Abrecht, J.-W. Chiou, J. Guo, D. Ariosa, S. N. Coppersmith, P. U. P. A. Gilbert, *Phys. Rev. B* **2008**, *77*, 064110.

[53] M. A. Meyers, P.-Y. Chen, M. I. Lopez, Y. Seki, A. Y. Lin, *J. Mech. Behav. Biomed. Mater.* **2011**, *4*, 626.

[54] M. A. Meyers, J. McKittrick, P.-Y. Chen, *Science* **2013**, *339*, 773.

[55] L. Pasquini, A. Molinari, P. Fantazzini, Y. Dauphen, J.-P. Cuif, O. Levy, Z. Dubinsky, E. Caroselli, F. Prada, S. Goffredo, *J. R. Soc. Interface* **2015**, *12*, 20150168.

[56] F. Barthelat, Z. Yin, M. J. Buehler, *Nat. Rev. Mater.* **2016**, *1*, 16007.

[57] J. Lastam, E. Griesshaber, X. Yin, U. Rupp, I. Sánchez-Almazo, M. Heß, P. Walter, A. Checa, W. W. Schmahl, *Sci. Rep.* **2023**, *13*, 2189.

[58] X. Su, A. M. Belcher, C. M. Zaremba, D. E. Morse, G. D. Stucky, A. H. Heuer, *Chem. Mater.* **2002**, *14*, 3106.

[59] S. Amini, M. Tadayon, S. Idapalapati, A. Miserez, *Nat. Mater.* **2015**, *14*, 943.

[60] Z. Deng, H.-C. Loh, Z. Jia, C. A. Stifler, A. Masic, P. U. Gilbert, R. Shahar, L. Li, *Acta Biomater.* **2022**, *137*, 147.

[61] a) A. C. Fischer-Cripps, *Introduction to Contact Mechanics*, Vol. *101*, Springer, Berlin, Germany **2007**; b) G. Anstis, P. Chantikul, B. R. Lawn, D. Marshall, *J. Am. Ceram. Soc.* **1981**, *64*, 533.

[62] a) S. Amini, A. Miserez, *Acta Biomater.* **2013**, *9*, 7895; b) C. Kearney, Z. Zhao, B. Bruet, R. Radovitzky, M. Boyce, C. Ortiz, *Phys. Rev. Lett.* **2006**, *96*, 255505.

[63] a) C. F. Böhm, P. Feldner, B. Merle, S. E. Wolf, *Materials* **2019**, *12*, 1630; b) M. E. Kunitake, L. M. Mangano, J. M. Peloquin, S. P. Baker, L. A. Estroff, *Acta Biomater.* **2013**, *9*, 5353.

[64] J. W. Dunlop, R. Weinkamer, P. Fratzl, *Mater. Today* **2011**, *14*, 70.

[65] E. Beniash, C. A. Stifler, C.-Y. Sun, G. S. Jung, Z. Qin, M. J. Buehler, P. U. P. A. Gilbert, *Nat. Commun.* **2019**, *10*, 4383/1.

[66] a) S. Babcock, X. Cai, D. Kaiser, D. Larbalestier, *Nature* **1990**, *347*, 167; b) R. Valiev, *Nat. Mater.* **2004**, *3*, 511; c) Y. M. Wang, T. Voisin, J. T. McKeown, J. Ye, N. P. Calta, Z. Li, Z. Zeng, Y. Zhang, W. Chen, T. T. Roehling, *Nat. Mater.* **2018**, *17*, 63.

[67] a) D. Smith, V. Vitek, R. Pond, *Acta Metall.* **1977**, *25*, 475; b) D. Hughes, N. Hansen, *Acta Mater.* **1997**, *45*, 3871; c) Y. Huang, F. Humphreys, *Acta Mater.* **2000**, *48*, 2017; d) K. G. Janssens, D. Olmsted, E. A. Holm, S. M. Foiles, S. J. Plimpton, P. M. Derlet, *Nat. Mater.* **2006**, *5*, 124; e) T. Frolov, S. Divinski, M. Asta, Y. Mishin, *Phys. Rev. Lett.* **2013**, *110*, 255502.

[68] U. G. Wegst, H. Bai, E. Saiz, A. P. Tomsia, R. O. Ritchie, *Nat. Mater.* **2015**, *14*, 23.

[69] a) X. Cui, A. L. Rohl, A. Shtukenberg, B. Kahr, *J. Am. Chem. Soc.* **2013**, *135*, 3395; b) A. G. Shtukenberg, C. T. Hu, Q. Zhu, M. U. Schmidt, W. Xu, M. Tan, B. Kahr, *Cryst. Growth Des.* **2017**, *17*, 3562.

[70] V. A. Fernandes, A. J. Müller, A. J. Sandoval, *J. Food Eng.* **2013**, *116*, 97.

[71] a) Y. Yang, M. Chen, H. Li, H. Li, *Eur. Polym. J.* **2018**, *107*, 303; b) B. A. Palmer, V. J. Yallapragada, N. Schiffmann, E. M. Wormser, N. Elad, E. D. Aflalo, A. Sagi, S. Weiner, L. Addadi, D. Oron, *Nat. Nanotechnol.* **2020**, *15*, 138.

[72] B. Miao, D. N. Wood, W. Bian, K. Fang, M. H. Fan, *J. Mater. Sci.* **1994**, *29*, 255.

[73] Y. Yang, L. S. de Moraes, C. Ruzié, G. Schweicher, Y. H. Geerts, A. R. Kennedy, H. Zhou, S. J. Whittaker, S. S. Lee, B. Kahr, *Adv. Mater.* **2022**, *34*, 2203842.

ADVANCED MATERIALS

Supporting Information

A Molecular-Scale Understanding of Misorientation Toughening in Corals and Seashells

Andrew J. Lew, Cayla A. Stifler, Alexandra Tits, Connor A. Schmidt, Andreas Scholl, Astrid Cantamessa, Laura Müller, Yann Delaunois, Philippe Compère, Davide Ruffoni, Markus J. Buehler,* and Pupa U. P. A. Gilbert*

Supporting Information for

A molecular scale understanding of misorientation toughening in corals and seashells

Andrew J. Lew[1,2], Cayla A. Stifler[3], Alexandra Tits[4], Connor A. Schmidt[3,5], Andreas Scholl[6], Astrid Cantamessa[4], Laura Müller[4], Yann Delaunois[7], Philippe Compère[7], Davide Ruffoni[4], Markus J. Buehler[1*], Pupa U. P. A. Gilbert[3,5,8,9]†[*]

1 Laboratory for Atomistic and Molecular Mechanics (LAMM), Massachusetts Institute of Technology, 77 Massachusetts Ave., Cambridge, MA 02139, USA
2 Department of Chemistry, Massachusetts Institute of Technology, 77 Massachusetts Ave., Cambridge, MA 02139, USA
3 Department of Physics, University of Wisconsin, Madison, WI 53706, USA
4 Mechanics of Biological and Bioinspired Materials Laboratory, Department of Aerospace and Mechanical Engineering, University of Liège, B-4000 Liège, Belgium
5 Department of Chemistry, University of Wisconsin, Madison, WI 53706, USA
6 Advanced Light Source, Lawrence Berkeley National Laboratory, Berkeley, CA 94720, USA
7 Laboratory of Functional and Evolutionary Morphology (FOCUS Research Unit) and Center for Applied Research and Education in Microscopy (CAREM), University of Liège, B-4000 Liège, Belgium
8 Departments of Materials Science and Engineering, Geoscience, University of Wisconsin, Madison, WI 53706, USA
9 Chemical Sciences Division, Lawrence Berkeley National Laboratory, Berkeley, CA 94720, USA.
† Previously publishing as Gelsomina De Stasio
* Corresponding authors Pupa Gilbert, Markus Buehler

Email: pupa@physics.wisc.edu, mbuehler@mit.edu

This PDF file includes:

Materials and Methods
Figures S1 to S12

Materials and Methods

Samples

Synthetic spherulites. Aragonite spherulites were prepared twice (preparations CAS 16 and CAS 33) for PIC mapping analysis and nanoindentation and SEM toughness measurements, respectively. Both times they were prepare identically, using the ammonium carbonate diffusion method, as described in Falini et al. [1] and Sun et al. [2]. Briefly, ammonium carbonate ($(NH_4)_2CO_3$) powder was allowed to sublimate and diffuse into beakers containing final concentrations of 1 mM $CaCl_2$ and 5 mM $MgCl_2$ to keep the $[Mg^{2+}]$ to $[Ca^{2+}]$ ratio at 5:1. A glass slide of approximately 1 cm x 1 cm area was placed into each beaker along with 10 mL of the mixed solution, and the beaker was then covered with aluminum foil and sealed tightly with Parafilm M (Bemis, Neenah, WI). Three pinholes were pierced through the aluminum foil at the start of the experiment to allow slow diffusion of ammonium carbonate vapor. Ammonium carbonate powder (~10 g) was placed in a separate beaker sealed and pierced the same way as the growth solution beakers. The solution and the ammonium carbonate were then placed inside a desiccator for 48 h at room temperature. The glass

slide on which the spherulites had grown was taken out of the solution, rinsed with ethanol, and air-dried. The spherulites were then scraped off the glass slide using a razor blade to prepare samples for further analyses. Beamtime: October 2021. Nanoindentation and SEM: November 2021-July 2022.

Spi1-5. *Stylophora pistillata* coral skeleton (Fig. 1A) was provided by Tali Mass, February 2016. The coral was collected from the Red Sea near Eilat, Israel. The skeleton had been bleached and dried before we received it. Beamtime: April 2021.

Hm spicules. *Herdmania momus* tunicate ascidians (Fig. 1B) were collected in 2004 in Eilat, Israel, at a depth of 15 m, and preserved in ethanol the Steinhardt Museum of Natural History, Tel-Aviv, Israel, and were provided to us by Noa Shenkar, still in ethanol. In July 2019, we bleached two entire tunicate ascidians for 2 weeks in covered Petri dishes, then collected the vaterite spicules at the bottom of the dish, rinsed them in ethanol twice, and mounted, under a stereomicroscope, onto embedding molds. Beamtime: August 2019.

Pm prisms. *Pinctada margaritifera* (Fig. 1C) were collected in 2004 from the Ferme Perlière Paul Gauguin, Rangiroa, French Polynesia. In 2021, a 1 cm x 1 cm portions of one shell valve were cut with a diamond saw, and mounted vertically onto embedding molds, to expose the shell cross-section for analysis of the prismatic layer in PEEM. Beamtime: April 2021.

Nacre samples were from 6 shells, 4 modern and 2 fossils. These are listed below.

Hrf3-10, others. *Haliotis rufescens* California red abalone (Fig. 4) shells were acquired from Monterey Abalone Company (Monterey, CA, USA). In 2020, SEM experiments revealed that the Hrf3 shell had perfectly formed spherulites. In 2021, a 1 cm x 1 cm portions of the Hrf3 shell were cut with a diamond saw, and mounted vertically onto embedding molds, to expose the shell cross-section for analysis in PEEM. Beamtime: April 2021. Other Hrf shells were analyzed for steady-state nacre in 2019.

Pm4-4. *Pinctada margaritifera* from the Lowenstam collection, courtesy of Steve Weiner, collected by Heinz Lowenstam in Palau in the late 1950s or early 1960s. Beamtime: October 2012, reprocessed in 2021. FoV 21 µm, hn= 533.3 eV.

Hrb1-2. *Haliotis rubra* from Spring Bay, Tasmania (served in a restaurant, cooked, in January 2011). Beamtime: Aug 2011. FoV 20 µm, hn= 289.4 eV.

Ah4-1, previously named **Ps4-1**. Miocene *Atrina harrisii* (fragment size: 5.5 cm). Courtesy of Susan Butts and Jessica Utrup, YPM, Yale University, New Haven, CT, USA. Catalogue number IP 527512: collected by Susan M. Kidwell in Saint Mary's Co, MD in 1978. Specimen collected from the top of Unit 1, Drumcliff Shell Bed, Choptank Formation (Middle Miocene ~13 Ma). For more information, see ref. [3]. Data from this shell's nacre were used only for the histograms in Fig. 3, where it is named Ps. Beamtime: January 2015. FoV 21 µm, hn= 533.5 eV.

Ps5-1. Late Cretaceous (Maastrichtian. ~66-million-year-old) *Pinna* sp. (fragment size: 8 cm). Courtesy of Neil Landman and Bushra M. Hussaini, American Museum of Natural History (AMNH), New York, NY, USA. Catalogue number 99982: collected by Neil Landman, Susan Klofak, Matt Garb, Remy Rovelli, and Corinne Myers on May 28, 2010, in Tippah, Co, MS. Specimen collected from the Owl Creek Fm, Selma Group (Maastrichtian ~66 Ma). A single fragment was used for PEEM (Ps5-1) analysis. For more information, see ref. [3]. Data from this shell's nacre were used only for the histograms in Fig. 3, where it is named Ps. Beamtime: January 2015. FoV 21 µm, hn= 533.5 eV.

Ar5-1: Modern *Atrina rigida* (size: 29 cm). Purchased from Gulf Specimen Marine Laboratory, Panacea, FL, USA. The living animal was collected at the beginning of September 2014 from St. Joseph Bay, Gulf County, FL (29° 43' 15" N / 85° 19' 39" W) from a collection depth of between 0.5 and 2.0 m, kept in a tank for 3-4 weeks, shipped live to Madison, WI and sacrificed on Sept. 30th, 2014. PEEM sample Ar5-1 was cut from the right valve of shell Ar5. Data from this shell's nacre

were used only for the histograms in Fig. 3, where it is named Ps. Beamtime: January 2015. FoV 21 μm, hn= 533.5 eV.

Geologic aragonite: Aragonite single-crystals from Sefrou, Morocco, were mounted with their *c*-axes either parallel, perpendicular, or at 45° from the indentation direction.

All samples (synthetic spherulites, biomineral, and geologic crystals) were embedded into EpoFix (EMS, Hatfield, PA, USA) in 1-inch round molds, polished with an AutoMet 250 Pro Grinder Polisher (Buehler, Lake Bluff, IL, USA) down to 50 nm Al_2O_3 nanoparticles (MasterPrep, Buehler, Lake Bluff, IL, USA), and analyzed with Polarized Light Microscopy (PLM). The best samples (e.g., the abalone shell that best showed spherulites in PLM) were identified using PLM and selected for PEEM analysis and nanoindentation.

For PEEM analysis, the selected samples were first trimmed to an EpoFix block size of 17 mm x 17 mm and 3 mm thickness, then coated with 1 nm Pt in the region of interest, and 40 nm Pt surround it [4]. Since at the O K-edge the maximum probing depth is 5 nm [5], 1 nm guaranteed conductivity and therefore stability at high voltage, but no significant attenuation of the signal from the underlying biomineral surface. Forty nm Pt surrounding the region of interest guaranteed a strong and stable electrical contact with the sample holder, which was floating at -18 kV during the PEEM experiment.

For nanoindentation and SEM, the selected samples were left as 1-inch rounds in EpoFix, and analyzed dry in selected positions for the macroscopic geologic crystal, and in random positions for nacre, coral skeletons, and synthetic spherulites.

All sample preparations were done in the Gilbert Group (GG) lab at UW-Madison, WI, USA.

PhotoEmission Electron Microscopy (PEEM)
PEEM experiments were done as described in [6], using the PEEM-3 instrument on beamline 11.0.1.1 at the Advanced Light Source, Lawrence Berkeley National Laboratory, Berkeley, CA, USA. The sample surface was mounted vertically, and the x-ray beam had a 60° incident angle (from the normal to the sample surface, which is also the PEEM optical axis).

PIC Mapping or Polarization-dependent Imaging Contrast Mapping
For PIC mapping [7], stacks of PEEM images were acquired at the oxygen K-edge carbonate π* peak energy of 534 eV [8], with linear polarization from the elliptically polarizing undulator (EPU) varying from horizontal to vertical in 5° steps (19 images/stack). This rotation occurs in the polarization plane, to which all PIC mapping angles are referred: the in-plane angle, represented by hue, and the off-plane angle, represented by brightness [9] in PIC maps. Black pixels have no polarization dependence, either because the material is not crystalline and dichroic, e.g., organic envelopes between calcite prisms in Fig. 1C, CoCs in Fig. 1A, large horizontal band of organic layer in Fig. 4, or embedding epoxy around vaterite spicules in Fig. 1B, or because the crystalline *c*-axis is pointing directly into the beam. This is the case for a few crystals on the right top third of the image in Fig. 1A, or the one at bottom right in Fig. 1D.

PIC maps in Fig. 1 have 20 nm lateral resolution [10], and pixels sizes either 56 nm (A-D) or 22, 20, or 21 nm (E, F, G) and probing depth either 3 nm or 5 nm (at the C or O K-edges: O in A-E,G, C in F)[5].

PIC maps of coral, nacre, vaterite spicules, and prisms were created from the aligned stacks with the GG macros [11], each PIC map having *max b*=150, the value where the brightest crystals are displayed at maximum brightness without saturating and non-crystals remain dark (*a, b,* and *c* are fit parameters during PIC mapping [11]). Setting *max b* to the same value is the best way to ensure that every PIC map is normalized identically. Thus, we calculated all angles and angular distances (orientations and misorientations) based on color PIC maps, all with *max b*=150 for all biominerals, instead of using the direct fit parameters *a, b, c*. Most of the PIC maps had 60 nm pixels, with a few having 20 nm, and one having 10 nm pixels.

The PIC maps were then loaded into the "Analyze1" code in MATLAB where the misorientation between adjacent regions was calculated for 3-15 region pairs for each PIC map, with most PIC maps having 10 ROI pairs. In cases where the ROI pairs did not span the entire area of the PIC map, regions were chosen to be representative of the area. For instance, if only a small portion of PIC map had high-angle boundaries, then only one of the region pairs was extracted across such boundaries.

The ROIs were selected in Adobe Photoshop® 2023. The first ROI in the pair was created by selecting an area in the PIC map using the Magic Wand tool with tolerance 20, which is 8% of the 0-255 tolerance levels provided by Adobe Photoshop 2023. Other tolerances were tested and excluded because were too small and therefore did not capture the recognizable morphological features of biominerals (e.g., stacks of nacre tablets, single coral skeleton fibers) or too large, and captured multiple features not single ones. Figures S1-S3 and their captions describe this process step-by-step. That selection was modified to match the geometry of the biomineral and exclude any imaging artifacts that were included in the original selection, e.g., scratches. The second ROI in the pair was created by again selecting with the Magic Wand an area, adjacent to the first and again modifying the selection as necessary to match the geometry of the biomineral. The second ROI was modified to ensure that it exactly bordered the first one with no overlap, as shown in Figs. S1-S3. The selection was filled in with white and the rest of the image was filled with black. All the ROI pairs were exported as PNG files using the Export Layers as Files option in Photoshop.

The PIC map and all the ROI pairs were loaded into the "Analyze1" code, which records the ROIs by storing the indices of the white pixels in each ROI mask file. The code then computes the average color in the two ROIs by averaging the squares of the R, G, and B values and taking the square root to prevent the average color being artificially lowered because of the non-linearity of the RGB scale. There are more sophisticated ways to compute the average color in an image, but since the regions were already very close in color, the additional accuracy made very little difference. The average colors for the two regions are converted into HSB colors and then to the in-plane and out-of-plane *c*-axis angles that the colors represent, using equations 1 and 2 below. This calculation is repeated for every ROI pair and the misorientation between each ROI pair is stored into an array of all misorientations.

The misorientation between the two regions is computed with equation 3 below. For spherulites within nacre and coral skeletons, only the misorientations within a spherulitic trabecula were considered for the analysis, so the high angle boundaries between abutting spherulites having different centers were excluded from this analysis. The misorientations for all region pairs for a given biomineral were plotted with "histograms3" code with 1°-wide bins and the percentages of each bin on the y-axis.

equation 1 $\quad c_{in-plane} = \dfrac{\pi}{2} - \pi * h, where\ h\ is\ the\ hue\ and\ 0 \le h \le 1$

equation 2 $\quad c_{out-of-plane} = \dfrac{\pi}{2} - \dfrac{\pi}{2} * B, where\ B\ is\ the\ brightness, with\ 0 \le B \le 1$

equation 3 $\quad \theta = \cos^{-1}[\sin c_{in-plane1} \cos c_{out-of-plane1} \sin c_{in-plane2} \cos c_{out-of-plane2}$
$$+ \sin c_{in-plane1} \sin c_{out-of-plane1} \sin c_{in-plane2} \sin c_{out-of-plane2}$$
$$+ \cos c_{in-plane1} \cos c_{in-plane2}]$$

All MATLAB code is available to any interested user upon request to the corresponding author.

Nanoindentation and Scanning Electron Microscopy (SEM)

All nanoindentation experiments were carried out at the University of Liège, Belgium, in the Ruffoni's Lab, termed Mechanics of Biological and Bioinspired Materials Laboratory, in the Department of Aerospace and Mechanical Engineering.

Two sets of nanoindentation experiments were performed on polished samples using a Triboindenter TI-950 (Bruker, USA). First, indentation with a low-load (10 mN) transducer was done using a standard Berkovich diamond probe (calibrated on fused quartz), a trapezoidal load function (10 seconds loading, 5 seconds holding, and 10 seconds unloading) and a reference peak load of 1500 µN (corresponding to a penetration depth of 80-180 nm). Low-load indentation was performed on at least three different locations per sample considering square grids from 9 to 25 indents each (depending on the sample), with indentation spacing of 5 µm. The main outputs of the low-load nanoindentation are the indentation elastic modulus (also called reduced modulus) E and the hardness H, quantified based on the load-depth curves using the standard Oliver-Pharr approach [12]. The local mechanical properties (E and H, presented in Fig. S5) are used as input for the fracture study.

In the second set of indentation experiments, the same samples were tested using a high load (10 N) transducer (3D OmniProbe, Bruker) equipped with a cube corner diamond probe. Again, a trapezoidal load-controlled function was used (5 s-5 s-5 s) and peak indentation load varied from 1 mN to 1500 mN. For each load, 5 indents were done with indent spacing adapted to the higher loads and ranging from 50 to 250 µm. Considering the small dimensions and the variability of the available surface area for indentation (due to sample embedding and polishing), synthetic spherulites were indented at a fixed peak load of 100 mN, which is high enough to induce detectable cracking but small enough to avoid splitting the spherulites into two or more pieces. Following high load indentation, the samples were gold coated (about 20 nm coating thickness) in a Balzers SCD-004 sputtering unit (BAL-TEC, Switzerland) and imaged in secondary electrons (SE) in a FEG-SEM Tescan Clara (Tescan, Czech Republic) at 15 kV (high vacuum, ET-detector). SE-SEM imaging was used to measure the radius of the residual indent R_I and the radius of the cracked/damaged region R_D from the center of the indent (a measure of crack length, thus, $c = R_D$), as shown in Fig. S6. For each indentation load, 2 to 5 indents were imaged. To estimate indentation fracture toughness, we fitted the correlation between crack length c and indentation load P (Fig. S7) obtained by rewriting the fracture toughness equation as described in [13]:

equation 4 $\quad c = \left(\frac{E}{H}\right)^{1/3} \left(\frac{\chi P}{K_c}\right)$

Materials with a known crystal anisotropy (geologic aragonite and nacre) were indented both perpendicular (Fig. 5) and parallel to the *c*-axis (Fig. S8).

MD Simulations

All MD simulations were done in the Buehler's Lab, termed Laboratory for Atomistic and Molecular Mechanics (LAMM), at Massachusetts Institute of Technology, Cambridge, MA, USA.

To model the effect of misorientation on the fracture behavior of aragonite, vaterite, and calcite, we represented the structure around grain boundaries as bicrystal samples consisting of two crystals stacked in the horizontal direction and subjected them to tensile loading in the vertical direction.

The left crystal had lattice coordinates rotated about the depth axis to the desired misorientation angle θ while the right crystal's orientation was kept fixed with the crystalline *c*-axis vertical, parallel to the loading direction [14]. A triangular notch 2 nm wide by 7 nm long was carved into the right face to serve as the initial crack. This 0.8 nm thick right face was constrained to forbid horizontal motion in order to enforce purely Mode I-fracture and eliminate shearing, which could significantly impact crack dynamics [15]. Additionally, Mode III-fracture was not observed. In doing so, our modeling setup focuses solely on the effect of the misorientation interface without other mechanisms that may also affect toughness. This sample setup is illustrated in Fig. 6A. Single-crystal fracture was similarly conducted as a comparative control, with the same setting but with only one crystal, with its *c*-axis oriented to an angle γ from the loading direction, as shown in Fig. S11A.

Simulations were run using the classical molecular dynamics (MD) code Large-scale Atomic/Molecular Massively Parallel Simulator (LAMMPS) [16]. Crystal equilibration and sintering were conducted with periodic boundary conditions. Mode I-fracture tensile tests were conducted with periodicity only in the depth-wise direction, with non-periodic conditions applied in the loading and crack propagation directions to remove the effects of lattice mismatch at the boundary and probe the effects of a single surface notch rather than infinite internal notches [14, 17]. Established force field parameters developed by Raiteri et al. [18] applicable to $CaCO_3$ were used. However, long range Coulombic solvers responsible for computing charge interactions in an infinite array of periodic images [16] were omitted for proper treatment of non-periodic systems.

Crystal coordinates for aragonite [19], vaterite [20], and calcite [21] were first equilibrated to 300 K and 1 bar. From equilibrated single crystal structures, misorientation grain boundaries were formed by constructing two grains with the desired orientations and sintering them together. Specifically, for each sample setup, we started with an equilibrated single crystal of the calcium carbonate polymorph under study. This single crystal was duplicated to instantiate a second crystal, which was placed along the negative horizontal direction relative to the first crystal with a gap of 5 Angstroms between the two. This left-hand crystal was then rotated about its center to the desired misorientation angle. This intermediate step results in a rotated left-hand crystal which leaves empty spaces in the overall sample along its faces, and it interpenetrates the first crystal in triangular regions at its corners. To address these problems, we first expanded this rotated crystal in the plane to cover these spaces by tiling it thrice in height and width, and subsequently cut down this expanded crystal to the proper rectangular region covered by the original non-rotated crystal to remove interpenetration of atomic coordinates. It should be noted that this process was carefully conducted to ensure that the system's charge neutrality is maintained. This process results in two rectangular crystal grains separated by a gap of 5 Ångstroms, wherein the left crystal has an internal atomic arrangement corresponding to the desired misorientation angle. Other than cutting the rotated crystal to restore the initial 5 Ångstrom gap, no other specific manipulation of the atoms at the surface of the gap was conducted. This initial gap is necessary to ensure that atomic coordinates do not overlap, which can prematurely introduce large stresses in the bicrystal sample and yield invalid simulations. To subsequently close this gap and form the interface, we brought these two separate crystals together via sintering. This sintering process consisted of four stages [22]: increasing pressure in the horizontal direction from 1 bar to 10 GPa over 10 ps to press the two crystals together, holding the pressure at 10 GPa for 10 ps, decreasing the pressure down to 1 bar over 10 ps, and then holding at 1 bar for 10 ps to allow relaxation of residual stresses. This four-stage sintering process was repeated three times to ensure a well-formed, energetically stable interface. Misorientations of 5°, 10°, 20°, 30°, 45°, 60°, 75°, and 90° were investigated, and Mode I-fracture of each misorientation case was run three times to account for differences from random thermal fluctuations.

To facilitate tensile fracture, 0.8 nm thick walls were pulled away from each other at a 10 m/s strain rate in a two-part process consisting of deformation and equilibration steps, repeated until fracture

completion [17, 23]. Specifically, we alternated between 0.5 ps of deformation with NVE ensemble to ensure energy conservation, and 1 ps of fixed sample length equilibration at 300 K with NVT ensemble, until a total strain of 10%.

Fracture Visualization

Visualization of atomic structure and fracture dynamics was also done at MIT-LAMM, with the Open Visualization Tool (OVITO) [24]. To aid in simplifying the visualization of crack paths, atomic positions were frozen to their initial positions and represented in greyscale. Then, fracture path images were obtained by coloring atoms according to the percentage of neighbors lost over the course of fracture - white corresponding to unperturbed crystal structure and black corresponding to atoms that have lost half of their neighbors (*i. e.* at newly created fracture surfaces). In this way, we could visualize the precise path along which the crystal structure failed.

References
[1]   G. Falini, S. Albeck, S. Weiner, L. Addadi, Science 1996, 271, 67.
[2]   C.-Y. Sun, M. A. Marcus, M. J. Frazier, A. J. Giuffre, T. Mass, P. U. Gilbert, ACS Nano 2017, 11, 6612.
[3]   P. U. P. A. Gilbert, K. D. Bergmann, C. E. Myers, M. A. Marcus, R. T. DeVol, C.-Y. Sun, A. Z. Blonsky, E. Tamre, J. Zhao, E. A. Karan, N. Tamura, S. Lemer, A. J. Giuffre, G. Giribet, J. M. Eiler, A. H. Knoll, Earth Plan Sci Lett 2017, 460, 281.
[4]   G. De Stasio, B. H. Frazer, B. Gilbert, K. L. Richter, J. W. Valley, Ultramicrosc 2003, 98, 57.
[5]   B. H. Frazer, B. Gilbert, B. R. Sonderegger, G. De Stasio, Surf Sci 2003, 537, 161.
[6]   P. U. P. A. Gilbert, in *Biomineralization Sourcebook, Characterization of Biominerals and Biomimetic Materials*, (Eds: E. DiMasi, L. B. Gower), CRC Press, Boca Raton, FL 2014, 135.
[7]   P. U. P. A. Gilbert, A. Young, S. N. Coppersmith, Procs Natl Acad Sci 2011, 108, 11350.
[8]   M. Nicholls, P. Norton, G. Bancroft, M. Kasrai, G. De Stasio, L. Wiese, Tribol Lett 2005, 18, 261.
[9]   P. U. P. A. Gilbert, *Physics in the Arts*, Academic Press, Cambridge, MA, USA 2021.
[10]   G. De Stasio, L. Perfetti, B. Gilbert, O. Fauchoux, M. Capozi, P. Perfetti, G. Margaritondo, B. P. Tonner, Rev Sci Instrum 1999, 70, 1740.
[11]   GG-Macros, http://home.physics.wisc.edu/gilbert/software.htm 2022.
[12]   W. C. Oliver, G. M. Pharr, J Struct Biol 1992, 7, 1564.
[13]   Z. Deng, H.-C. Loh, Z. Jia, C. A. Stifler, A. Masic, P. U. Gilbert, R. Shahar, L. Li, Acta Biomater 2022, 137, 147; A. Miserez, J. C. Weaver, P. J. Thurner, J. Aizenberg, Y. Dauphin, P. Fratzl, D. E. Morse, F. W. Zok, Adv Funct Mater 2008, 18, 1241.
[14]   W. Fang, H. Xie, F. Yin, J. Li, Q. Fang, Mat Sci Eng A 2016, 666, 314.
[15]   M. J. Buehler, A. Cohen, D. Sen, J Algor Comp Tech 2008, 2, 203.
[16]   S. Plimpton, J Comp Phys 1995, 117, 1.
[17]   W. Velilla-Diaz, A. Pacheco-Sanjuan, H. R. Zambrano, Comp Mater Sci 2019, 167, 34.

[18]   P. Raiteri, R. Demichelis, J. D. Gale, J P Chem C 2015, 119, 24447; P. Raiteri, J. D. Gale, D. Quigley, P. M. Rodger, J P Chem C 2010, 114, 5997.
[19]   D. Jarosch, G. Heger, Tschermaks mineralogische und petrographische Mitteilungen 1986, 35, 127.
[20]   S. R. Kamhi, Acta Crystallogr 1963, 16, 770.
[21]   R. J. Reeder, D. J. Barber, *Carbonates: mineralogy and chemistry*, Vol. 11, Mineralogical Society of America Washington, DC, 1983.
[22]   E. Beniash, C. A. Stifler, C.-Y. Sun, G. S. Jung, Z. Qin, M. J. Buehler, P. U. P. A. Gilbert, Nat Comms 2019, 10, 4383/1.
[23]   S. Chandra, N. N. Kumar, M. Samal, V. Chavan, S. Raghunathan, Comp Mater Sci 2017, 130, 268.
[24]   A. Stukowski, Mod Sim Mat Sci Eng 2009, 18, 015012.
[25]   B. Bruet, H. Qi, M. Boyce, R. Panas, K. Tai, L. Frick, C. Ortiz, J Mater Res 2005, 20, 2400; M. A. Meyers, A. Y.-M. Lin, P.-Y. Chen, J. Muyco, J Mech Behav Biomed Mater 2008, 1, 76.
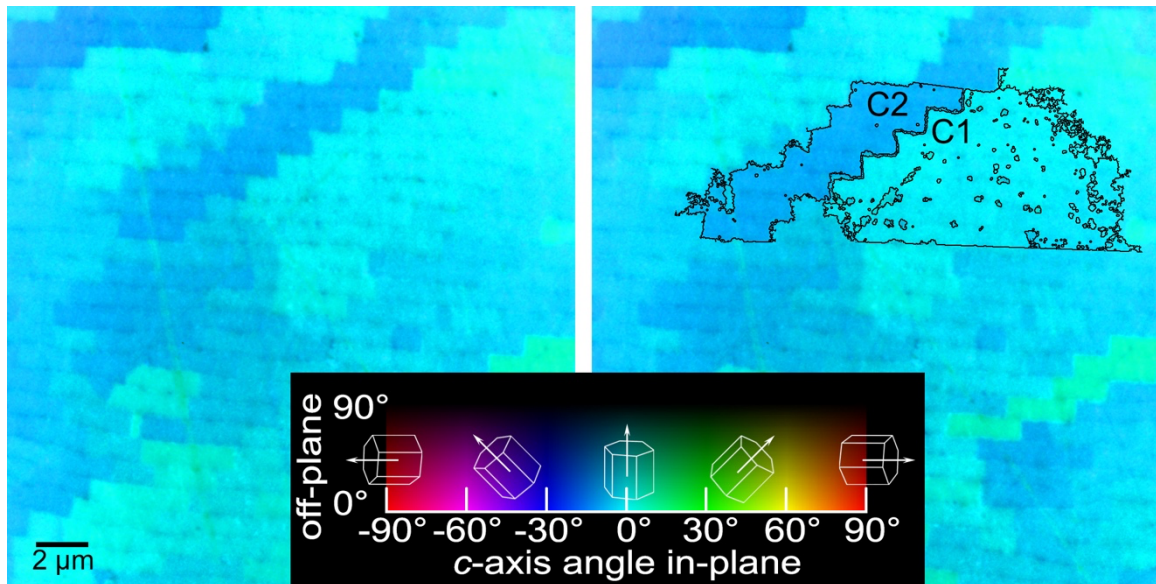
Figure S1: A PIC map of *Pinctada margaritifera* nacre, indicating 2 adjacent regions of interest (ROIs) forming "a pair". The orientation of the *c*-axis in both C1 and C2, displayed as hue and brightness in this PIC map, is averaged over the whole ROI, then, the misorientation of the C1 and C2 c-axes is measured. Each ROI is selected using the Magic Wand in Adobe Photoshop® 2023, with tolerance 20, which works best to capture tablet stacks of co-oriented tablets in nacre, or spherulitic fibers in coral skeletons. ROIs C1 and C2 are outlined here for clarity. The measurement uses every pixel in the solidly white ROI, as shown in Fig. S2.
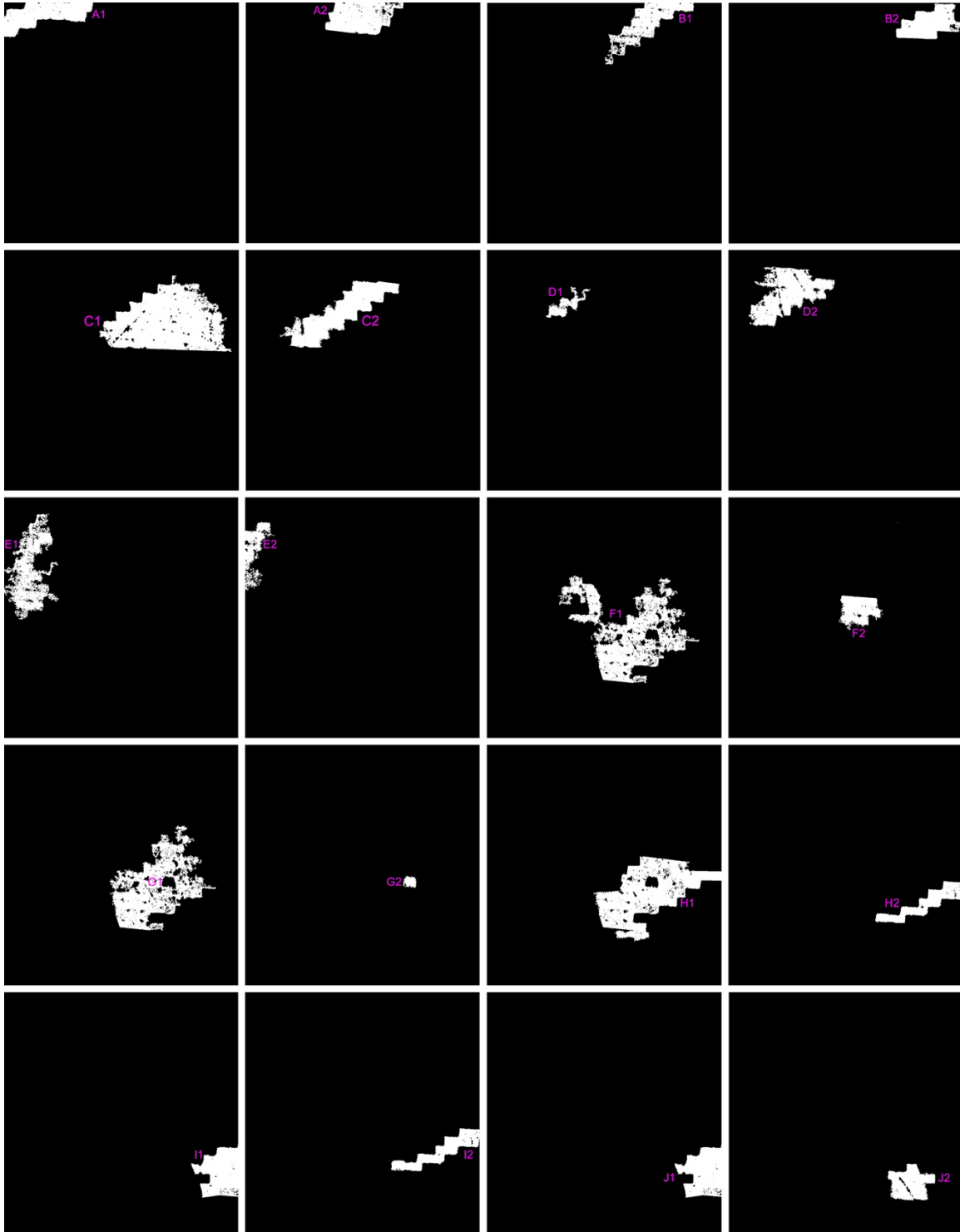
Figure S2: All pairs of regions of interest (ROIs) in the area of nacre displayed in Fig. S1. By selecting all discernible ROIs in each biomineral area, and multiple areas per sample, statistical significance can be achieved. Each pair is identified by a letter, each ROI in a pair has a number, e.g. A1 and A2, B1 and B2, etc. Across all biominerals and synthetic spherulites, we analyzed 1664 ROIs.
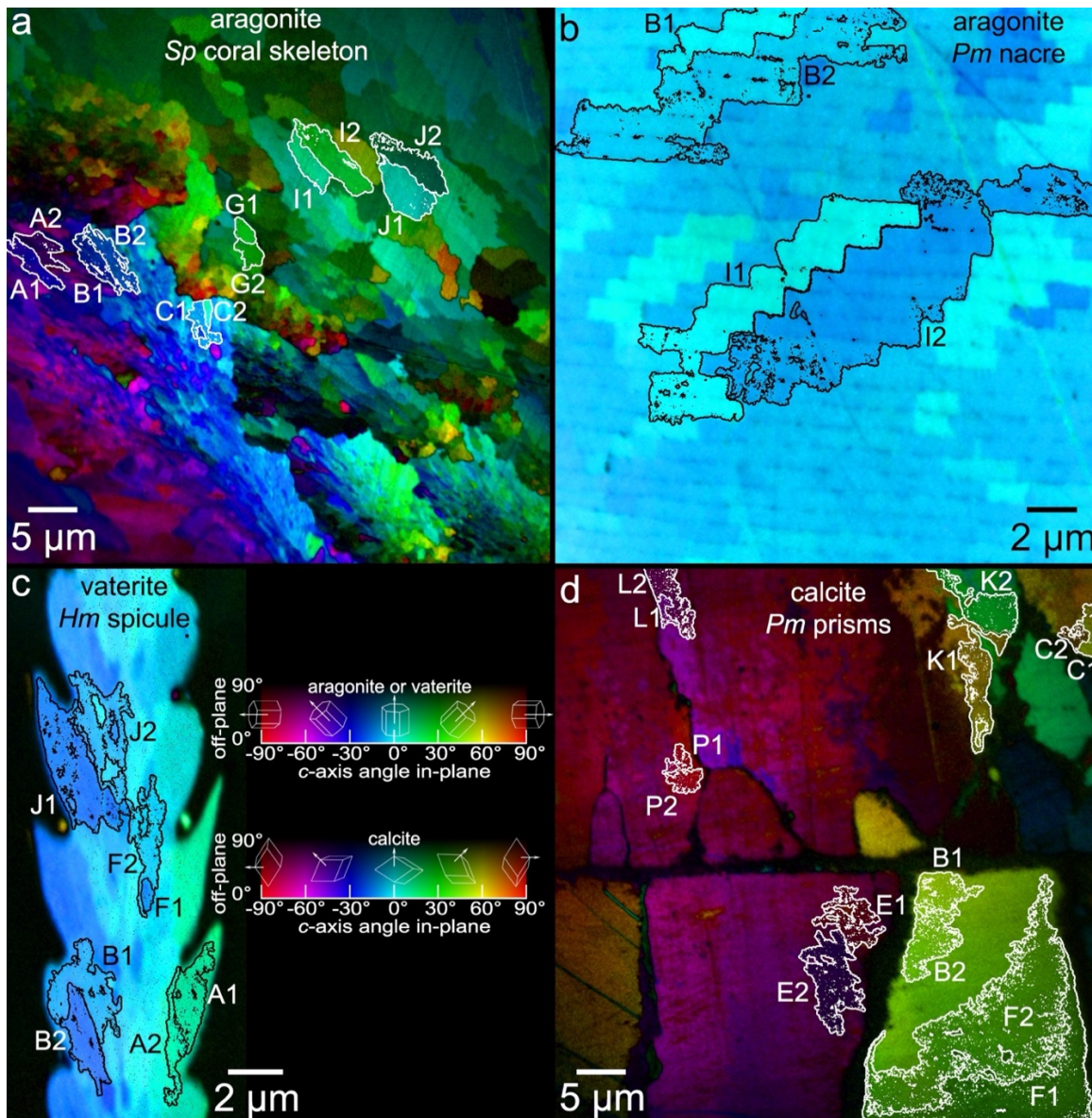
9

Figure S3: Example in all biominerals of pairs of regions of interest (ROIs) within which misorientation was measured. Each two adjacent crystallites are labelled with the same letter and two numbers, e.g., A1&A2 are a pair of adjacent crystallites. These are examples of a few pairs, all crystallites in each image were paired and analyzed. In Adobe Photoshop® the Magic Wand tool with a tolerance of 20 was used to define each ROI. Each ROI was defined manually clicking on each crystallite and eliminating portions of the ROI inconsistent with our knowledge of the biomineral, e.g., a border around multiple nacre tablets in a stack, or, in a coral skeleton, two crystallites in two distinct bundles of spherulitic acicular crystals (trabeculae), selected by the Magic Wand because they happen to have the same orientation, but from their shape and position one can see that they are clearly distinct crystallites. Once the two adjacent ROIs in a pair were selected, misorientation angle   between the two ROIs' *c*-axes was measured using MATLAB. This is possible because the orientation of the *c*-axis in each ROI is quantitatively represented by color in PIC map, where color includes hue and brightness, which display the in-plane and off-plane angles of the *c*-axis in 3D-space. The biominerals shown here are (a) an aragonite coral skeleton from *Stylophora pistillata* (*Sp*), a portion of the aragonite nacre layer (b) and a portion of the calcite prismatic layer (d) from *Pinctada margaritifera* (*Pm*), and (c) a vaterite spicule from *Herdmania momus* (*Hm*). Notice that, where the misorientation of adjacent crystallites is larger, an organic

layer is present, which appears black in PIC mapping because these organics are disordered and therefore do not have a polarization dependence. Dark layers are evident here between distinct trabeculae in the *Sp* coral skeletons in (a), between prisms in *Pm*, and within prisms (panel d here, and Fig. 1C).
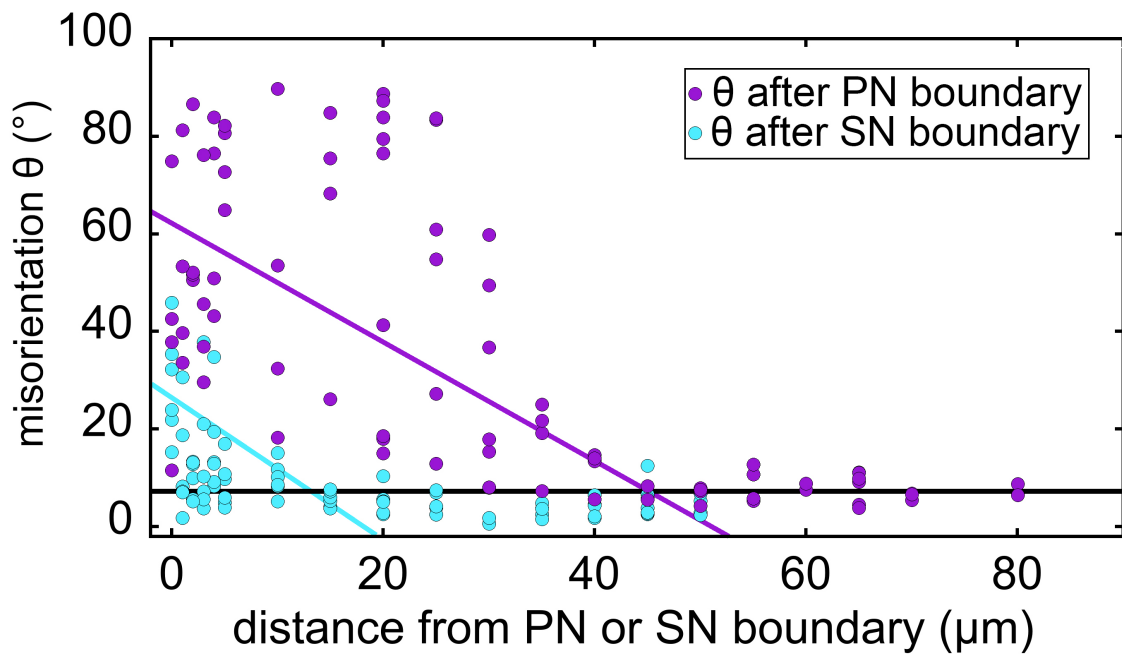

Figure S4: Misorientation decay after the prismatic-nacre (PN) or spherulites-nacre (SN) boundary in *Hrf* nacre. The misorientation of *c*-axes of each pair of adjacent nacre tablet crystals, plotted vs. the distance from either the PN or the SN boundary, defined as the position of the first recognizable tablet layer right after each boundary. The misorientations are smaller at the SN than the PN boundary (max 45° vs. max 90°), and they decay faster, within ~20 µm vs. ~50 µm. After these distances, growth continues as steady state nacre with ~10° misorientations in California red abalone (*Hrf*). Purple and cyan lines indicate linear fits obtained selecting only the data before convergence to steady state. The black line indicates steady state misorientation of adjacent tablets after convergence to steady state, which is ~10° in *Hrf*.
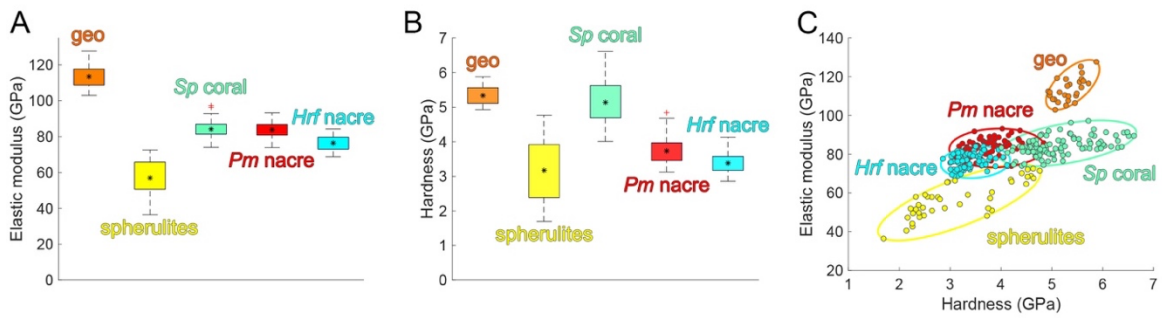
Figure S5. Indentation modulus and hardness of geologic, synthetic, and biogenic aragonites. A. Elastic modulus and B. hardness for the different aragonite minerals as measured by nanoindentation at a peak load of 1500 µN. Coral skeletons show the highest hardness. E and H mean ± Standard Deviation measured in multiple locations within each sample, except for synthetic spherulites, where different spherulites and locations were measured across multiple samples, because the spherulites are small (<50 µm in diameter). C. Ashby plot of the indentation elastic modulus versus hardness, offering a complementary view on the mechanical data.
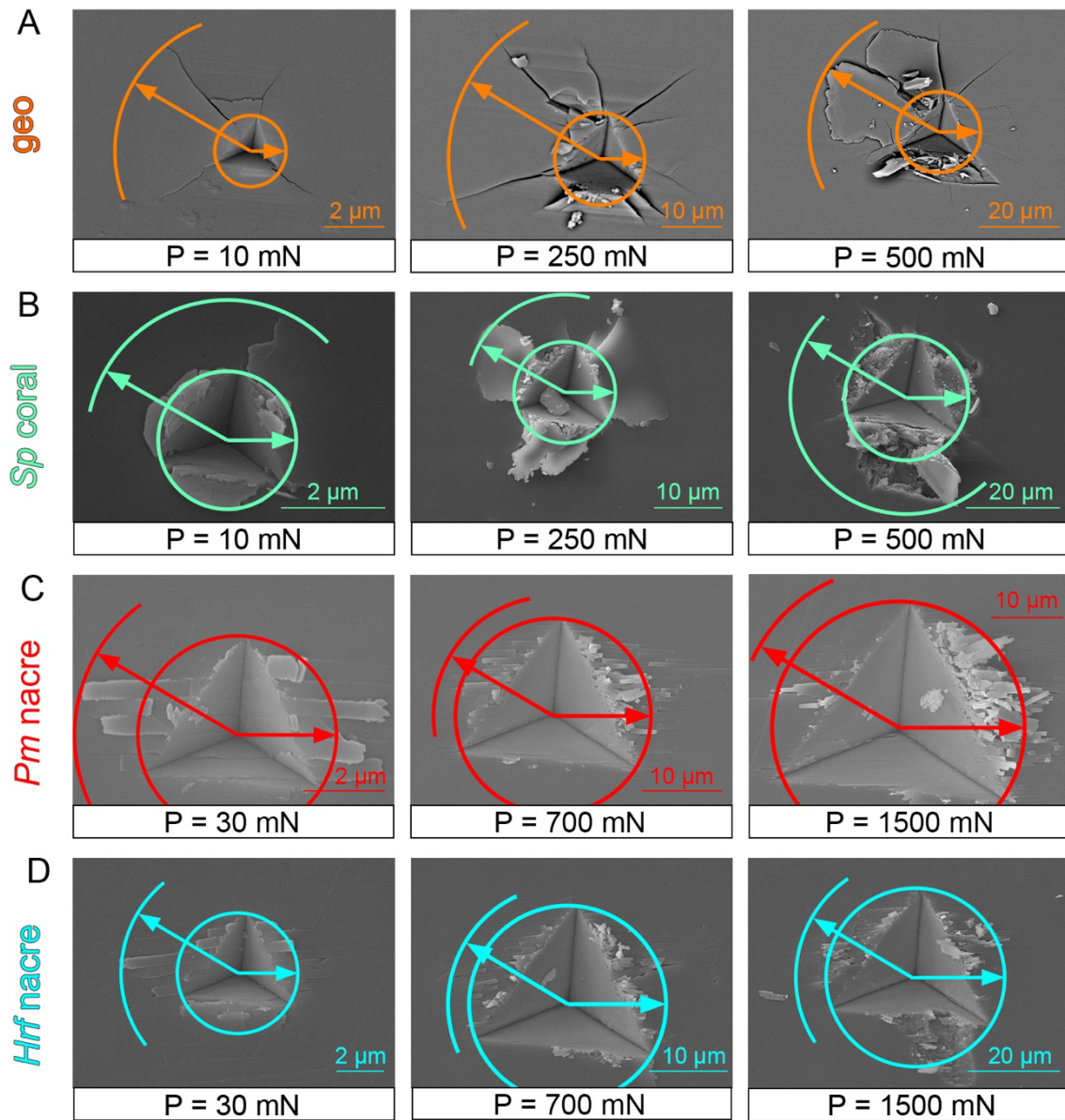
Figure S6. Indentation fracture: residual indents and surface damage. SEM images acquired post-indentation at increasing peak load of A. geologic aragonite (indented perpendicular to *c*-axis), B. coral skeleton, C. *Pm* nacre and D. *Hrf* nacre. Already at an indentation load *P* = 10 mN, geologic aragonite shows substantial tensile cracking. Coral skeletons have more intricate damage mechanisms, combining tensile cracking with shear-induced damage, the latter being dominant at higher loads. Nacre (tested perpendicular to *c*-axis) features completely different damage patterns, characterized by tablet sliding and pull out. At higher loads only, localized chipping and fractures are observed in nacre.
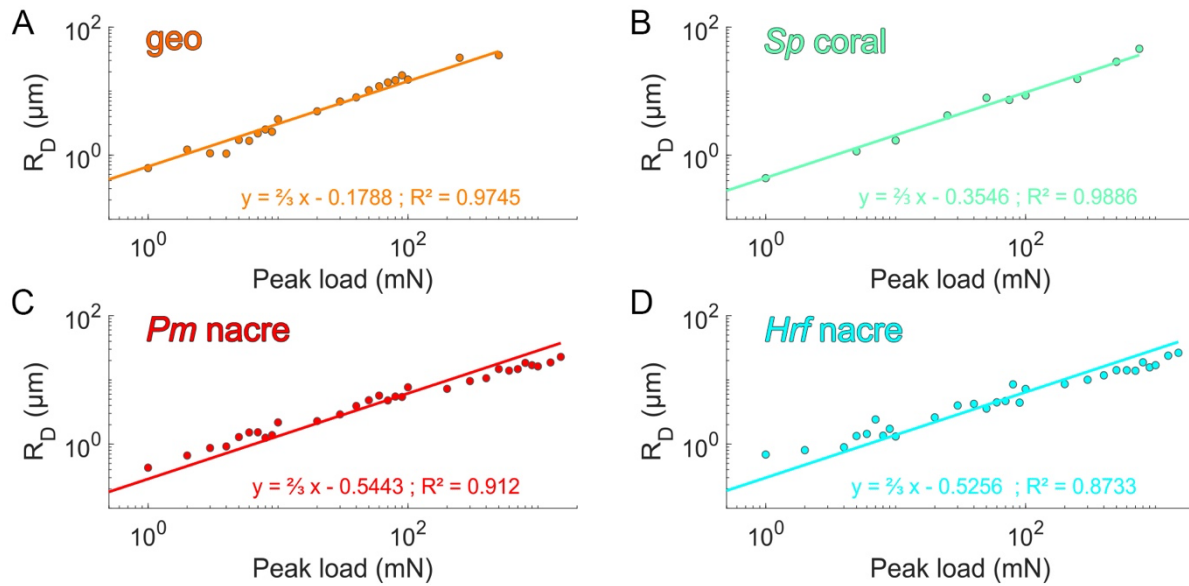
13

Figure S7. Correlation of crack length and indentation load with a cube-corner probe. The solid lines are linear fits, demonstrating the excellent correlation ($R^2>0.85$, calculated with linear regression using MATLAB) of indentation peak load and damage radius (a measure of crack length, thus $c = R_D$) used to calculate indentation fracture toughness as described in [13] and in the Methods. A. geologic, B. coral, C. *Pm* nacre and D. *Hrf* nacre. All fits have a constant slope of 2/3 and indentation fracture toughness is estimated based on the intercept.
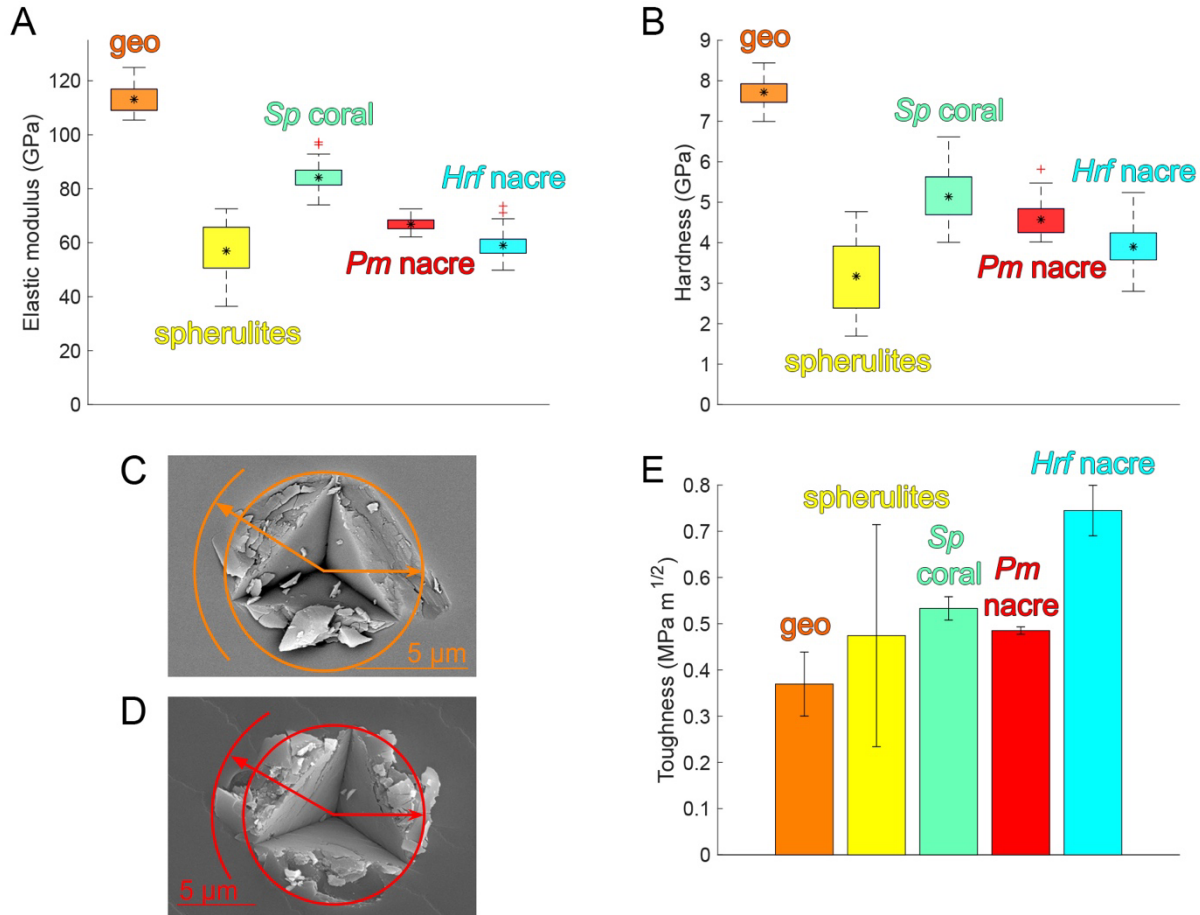
Figure S8. The anisotropic response of geologic aragonite and nacre does not change the message: systems with slight misorientations have greater indentation fracture toughness than single-crystal geologic aragonite also when indenting parallel to the *c*-axis. A. Indentation elastic modulus and B. hardness when probing geologic aragonite and nacre parallel to the *c*-axis. Data from synthetic spherulites and *Sp* coral skeletons are the same as in Fig. 5. Both geologic aragonite and nacre show anisotropic mechanical behavior. C-D. Post indentation SEM analysis (at 100 mN peak load) highlights different damage patterns obtained from indentation parallel to the *c*-axis: in geologic aragonite, damage appears as chipping and shear cracking rather than as long tensile cracks (Fig. 5A). In this configuration, loads higher than 500 mN are needed to propagate tensile cracking. At this threshold value, $R_D/R_I \approx 2$, which is the minimum ratio obtained from geologic aragonite when indenting perpendicular to *c*-axis (Fig. 5F). Only loads higher than 500 mN are, therefore, used to calculate indentation fracture toughness for geological aragonite. Nacre indented parallel to the *c*-axis here is less damage resistant, presumably because the toughening mechanisms provided by the organic sheets are less active, as suggested previously [25]. E. Despite these anisotropies, also when indenting parallel to the *c*-axis synthetic spherulites, coral skeletons, and nacre have higher indentation fracture toughness than single crystal geologic aragonite. The only minor difference between these data and Fig. 5 is that *Hrf* nacre is tougher than *Pm* nacre when measured with indentation parallel to *c*-axis (E), and less tough than *Pm* nacre when indentation is perpendicular to *c*-axis (Fig. 5). Data presented as mean ± SD over multiple locations within the same sample, except for synthetic spherulites, where different spherulites and locations were measured across multiple samples, because the spherulites are small (<50 μm in diameter).
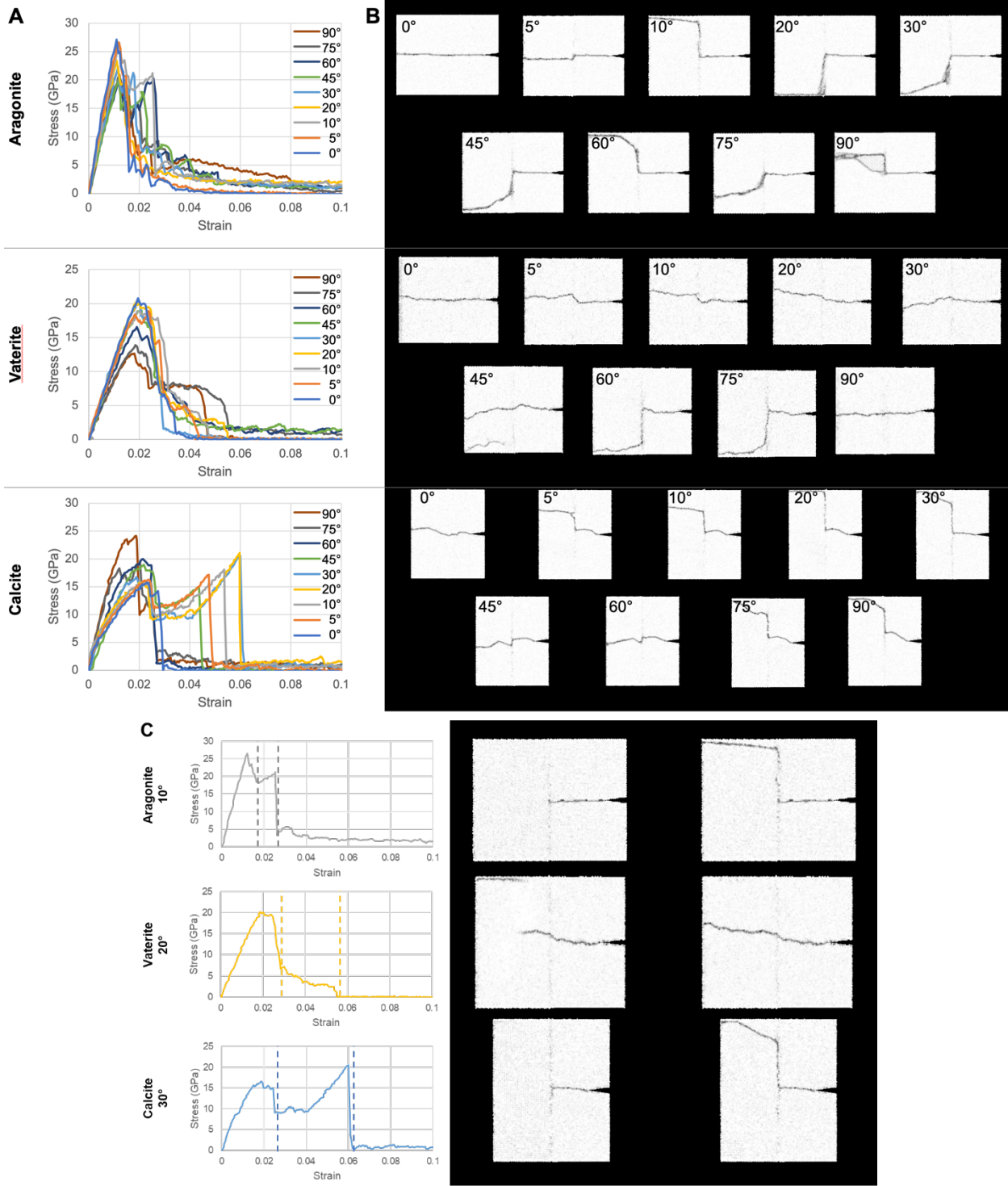
Figure S9: Bicrystal fracture behavior in MD simulations.
Fracture data for aragonite, vaterite, and calcite including A. stress-strain curves and B. fracture paths obtained for misorientation angles 0°, 5°, 10°, 20°, 30°, 45°, 60°, 75°, and 90°. C. Closer inspection of the peak misorientation toughening cases shows multi-stage crack evolution, with an initial crack corresponding to the first decrease in stress followed by further crack evolution for final relaxation. Notice that for vaterite, while the path does not qualitatively deflect in space like aragonite and calcite, there are two distinct stages of fracture. This is apparent in the stress strain curve, where stress does not immediately go to 0 after the first peak. Instead, stress persists for a

16

while until a second drop in stress at strain 0.055, indicating the second fracture. Thus, there is a delay in time and not simply one fracture event. Furthermore, the crack morphology at the first stress drop shows a secondary crack at the top of the structure. When transitioning to the final crack morphology, this area reforms and instead the crack goes through the center. In some sense, this initial path was "deflected" from the top edge to the center after final crack evolution.

We do not know why vaterite behaves differently from aragonite and calcite. But, this different qualitative behavior illustrates how general the quantitative effect of misorientation toughening is. Even in different crystal structures, which may respond to fracture in many different qualitative ways, small angle misorientations quantitatively persist as a toughening mechanism.
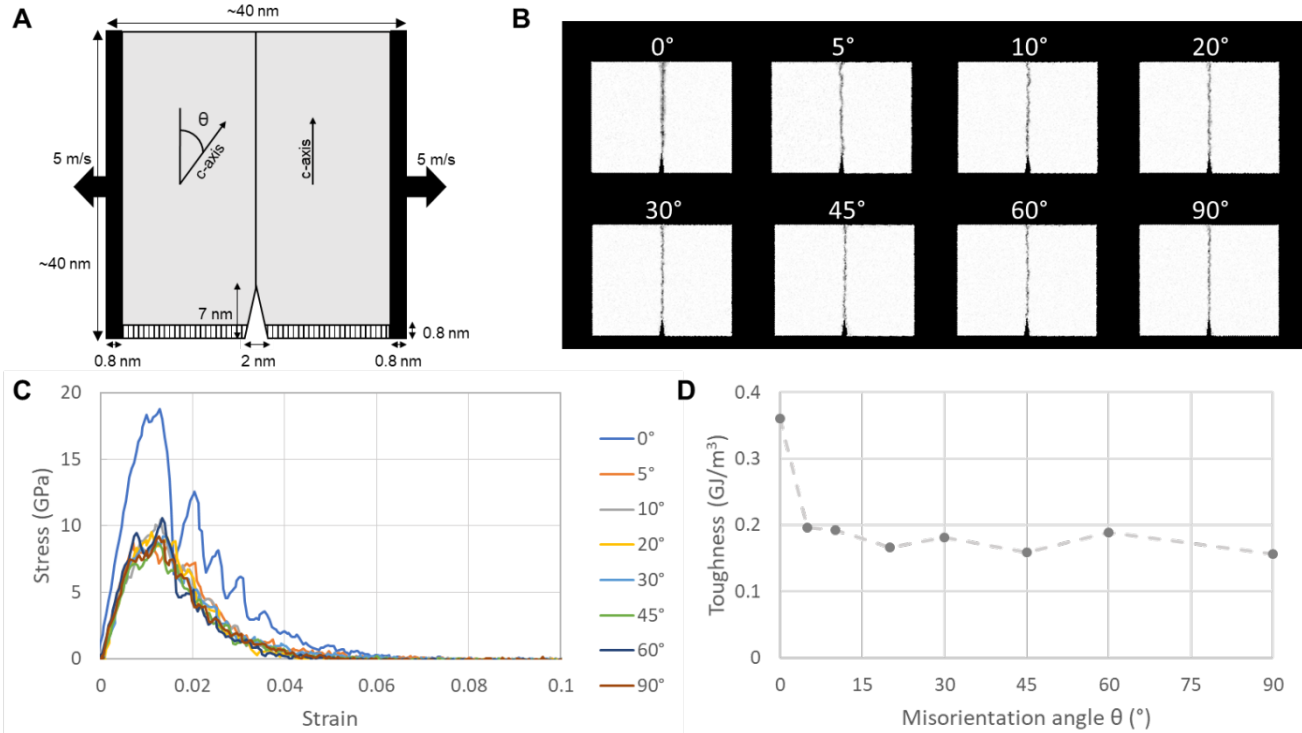

Figure S10: No toughening in the normal direction in MD simulations.
A. Aragonite was additionally subject to mode I fracture in the direction normal to the interface, with the right crystal *c*-axis perpendicular to the tensile direction and the left crystal *c*-axis rotated in the plane of the figure by a misorientation angle θ. B. Fracture paths for each case followed along the interface with stress-strain behavior given in panel C. D. The toughness is the same at any θ for misoriented bicrystal, only the single crystal toughness is higher, and in fact higher than when single crystals are notched and pulled along the *c*-axis (Fig. 6, 0° data points).
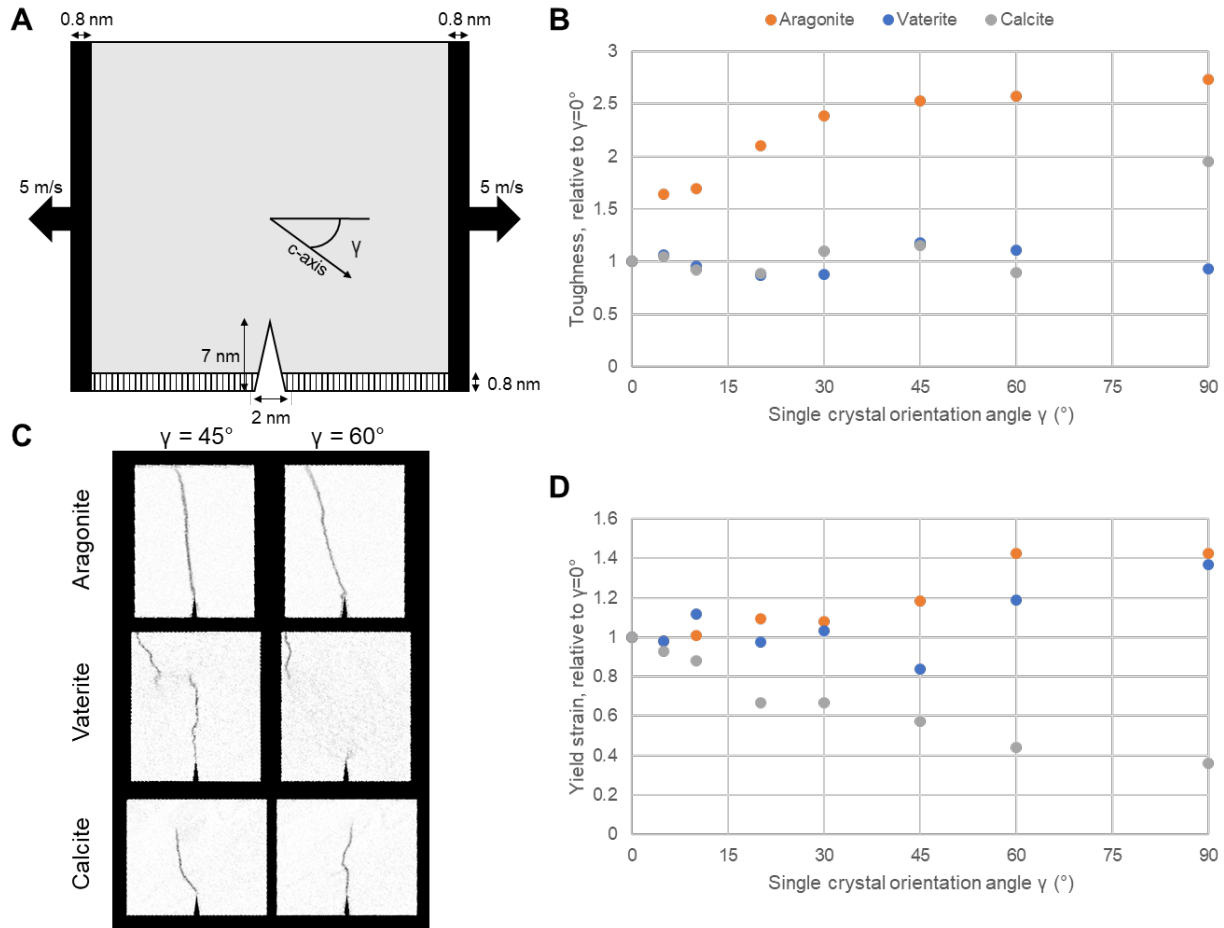
Figure S11: Single-crystal fracture behavior, distinct from the slight misorientation effect.
When the tensile load is applied at higher angles from the *c*-axis, e. g. $\gamma > 30°$, the path tortuosity of the crack can increase due to mechanisms other than slight angle misorientation toughening. This behavior can be understood in terms of (A) single crystal fracture, with crystal orientation γ. In the case of aragonite (B), this is because single-crystal toughness increases as the single-crystal is rotated to higher angles. For the case of vaterite (C), single crystals exhibit secondary fracture from the upper plane when rotated to higher angles such as $\gamma = 45°$ or 60°. And for the case of calcite (D), the yield strain decreases with rotation angle, favoring premature failure of the upper crystal as another mechanism of secondary fracture.
These single-crystal effects result in some path tortuosity in the bicrystal structures at higher misorientation angles, distinct from the slight misorientation effect.
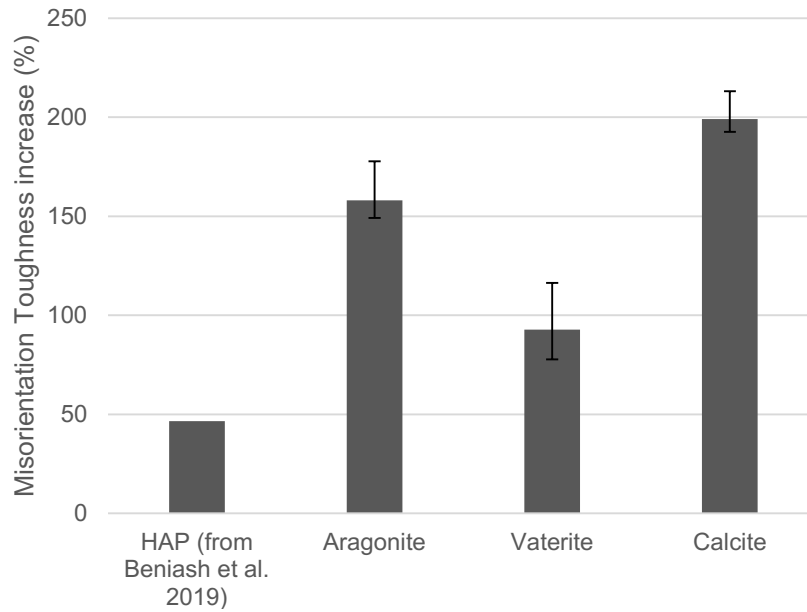
Figure S12: Slight misorientation plays a major role on toughness of bicrystals: it makes them 2x-3x tougher.
The percent increase in toughness from single crystal to slightly misoriented bicrystals shows that peak fracture toughness values more than double for aragonite, vaterite, and calcite. Calcite experiences the greatest change in toughness, reaching values approximately triple the single crystal case. The slight misorientation angle effect previously identified in the literature for hydroxyapatite (HAP) is shown for comparison.